

# The geometry of optimally transported meshes on the sphere

Chris J. Budd<sup>1,\*</sup>, Andrew T. T. McRae<sup>1</sup>, and Colin J. Cotter<sup>2</sup>

<sup>1</sup>*Department of Mathematical Sciences, University of Bath, Bath, BA2 7AY, UK*

<sup>2</sup>*Department of Mathematics, Imperial College London, London, SW7 2AZ, UK*

*\*Correspondence to: c.j.budd@bath.ac.uk*

Mesh redistribution methods provide meshes with increased resolution in particular regions of interest, while requiring that the connectivity of the mesh remains fixed. Some state of the art methods attempt to explicitly prescribe both the local cell size and their alignment to features of the solution. However, the resulting problem is overdetermined, necessitating a compromise between these conflicting requirements. An alternative approach, extolled by the current authors, is to prescribe only the local cell size and augment this with an optimal transport condition. It is well-known that the resulting problem is well-posed and has a unique solution, not just in Euclidean space but also on the sphere. Although the optimal transport approach abandons explicit control over mesh anisotropy, previous work has shown that, on the plane, the meshes produced are naturally aligned to various simple features. In this paper, we show that the same is true on the sphere. Furthermore, formal results on the regularity of solutions to optimal transport problems imply the sphere is actually more benign than the plane for mesh generation, due to its intrinsic curvature. We also see informal evidence of this. We provide a wide range of examples to showcase the behaviour of optimally transported meshes on the sphere, from axisymmetric cases that can be solved analytically to more general examples that are tackled numerically. Evaluation of the singular values and singular vectors of the mesh transformation provides a quantitative measure of the mesh anisotropy, and this is shown to match analytic predictions.

**Keywords:** Mesh adaptation, optimal transport, mesh alignment, Monge–Ampère equation

## 1. Introduction

Many partial differential equations are naturally formulated on the sphere,  $S^2$ , or on a thin spherical shell. A notable example is those equations describing atmospheric or oceanic flows on the

Earth, which are essential in weather forecasting and similar applications. To find approximate solutions to these, it is common to first define a mesh on the sphere (perhaps extended in vertical columns in the case of a thin shell). The equations are then discretized with respect to this mesh, using, for example, a finite difference or finite volume method.

There are many considerations for constructing a suitable mesh. At the very least, the mesh must be a reasonable approximation of the analytic domain. It is usually important that the solution can be faithfully represented on the mesh; this may be non-trivial if the solution develops small-scale features that move around over time. Issues can arise from interactions between the mesh and the numerical method being used, as described in Staniforth and Thuburn (2012), where the desirability of particular degree-of-freedom ratios between different fields (such as air pressure and wind speed) leads to constraints on the topology of the mesh. Furthermore, if computational efficiency is important, a structured mesh is desirable. These allow direct addressing to be used, and so generally lead to faster calculations than unstructured meshes (although the difference can be minimised in the spherical shell case since the radial direction always provides exploitable structure, even if the ‘horizontal’ mesh is unstructured (MacDonald et al., 2010; Bercea et al., 2016)).

The meteorological community have traditionally used a latitude–longitude mesh of the sphere, in which the sphere is divided into cells by lines of constant latitude and constant longitude. This mesh has the advantages of being fully structured and of having quadrilateral cells and orthogonal gridlines, which are beneficial for certain numerical schemes. However, the severe resolution clustering at the poles turns out to be problematic for numerical methods and for parallel efficiency. As a result, more uniform meshes have been considered, particularly in recent years (Williamson, 2007; Staniforth and Thuburn, 2012). These include varieties of cubed-sphere mesh as well as non-quadrilateral meshes such as triangular meshes derived from subdividing the faces of an icosahedron. Both cubed-sphere and icosahedral meshes can be represented as a collection of structured patches.

The standard varieties of these meshes are fairly uniform, with cell areas that vary by at most a factor of two. These are, therefore, not immediately suitable for resolving small-scale local features. We can generalise to using meshes that are similar to these, but which also make use of some form of redistribution or local refinement strategy to increase the resolution in particular regions. For atmospheric flows, this may be appropriate when the solutions of the governing PDEs develop small-scale features such as atmospheric fronts.

In recent papers (Weller et al., 2016; McRae et al., 2017), we considered an  $r$ -adaptive strategy for producing adapted meshes on the sphere. This used an optimal transport approach to produce meshes with the desired (spatially-varying) density of mesh points. That paper was primarily computational. In this companion paper, we look at the geometry and regularity of the resulting meshes generated using optimal transport methods. These methods have the advantage that they deliver meshes of provable regularity through the use of robust algorithms which are relatively simple to implement. They also have significant flexibility in the control of the mesh points.

This paper is structured as follows. In section 2, we introduce some basic theory of  $r$ -adaptive mesh relocation strategies, based on controlling the density of mesh points. We also describe

some measures of mesh quality. In section 3, we consider the construction of meshes on the sphere, and possibly more general two-dimensional Riemannian manifolds. This is achieved through the use of optimal transport maps from the sphere to itself, obtained by solving scalar partial differential equations of Monge–Ampère type. We also derive some a priori estimates of mesh regularity that follow from the analytic theory of optimally transported maps. A surprising conclusion is that meshes on the sphere tend to have better formal regularity than analogous meshes on the plane. In section 4, we show that the optimal transport problem is tractable in the axisymmetric case, and give analytic expressions for the resulting map and associated mesh quality measures. In section 5, we then consider specific axisymmetric examples. We construct corresponding meshes, obtained by applying the optimal transport maps to some common meshes of the sphere, including latitude–longitude, cubed-sphere and icosahedral. We also present analytically-derived and numerically-calculated quality measures for these meshes. In section 6, we briefly compare a spherical example to a ‘matching’ planar example, and show that the geometry of the sphere leads to a higher mesh quality. In section 7, we provide more general computational examples on the sphere, and show that the resulting meshes are naturally aligned to the prescribed features. Finally, in section 8, we draw some conclusions and consider future work.

## 2. Mesh construction and geometrical measures

### 2.1. Mesh construction

In this paper, we will always be considering an  $r$ -adaptive approach, in which mesh points are relocated while the topology remains unchanged. Suppose that we wish to construct a mesh  $\tau_P$  for simulating a physical problem in a domain  $\Omega_P$ , where  $\Omega_P$  lies in a manifold  $M$ . We assume that  $\tau_P$  will be specially adapted for the problem and may be highly non-uniform. In this work, we are particularly interested in the case where  $M$  is the sphere  $S^2$ , with  $\Omega_P = M$ . However, we will frequently draw comparisons to the planar case  $M = \mathbb{R}^2$ . Previous work on this planar case can be found in Budd et al. (2015).

We also define a ‘computational’ domain  $\Omega_C \subseteq M$ , with a computational mesh  $\tau_C$ . We assume the cells of  $\tau_C$  are reasonably uniform—perhaps fully uniform in the planar case—having shapes and sizes that do not vary too much. This is the case in an icosahedral mesh on the sphere refined through repeated bisection, and in a gnomonic cubed-sphere mesh. In the  $r$ -adaptive approach, we assume the existence of a bijective map  $F : \Omega_C \rightarrow \Omega_P$ , with  $\tau_P$  the image of  $\tau_C$  under the action of this map. It follows that  $\tau_P$  will have the same topology (connectivity) as  $\tau_C$ .

We use  $\vec{\xi}$  to denote a position vector in  $\Omega_C$ , and  $\vec{x}$  to denote the corresponding position in  $\Omega_P$ :  $F(\vec{\xi}) = \vec{x}$ . Let  $U$  be a small open set containing  $\vec{\xi}$ , and let  $V$  be the image of this set under the action of  $F$  (hence containing  $\vec{x}$ ). We may compute the ratio of the volumes (areas) of these two sets,  $|V|/|U|$ . In the limit  $|U| \rightarrow 0$ , we define

$$r(\vec{\xi}) = \lim_{|U| \rightarrow 0} \frac{|V|}{|U|} \quad (2.1)$$

to be the limiting area ratio. If  $M = \mathbb{R}^2$ , we have

$$r(\vec{\xi}) = |\det J|, \quad (2.2)$$

where  $J$  is the Jacobian of the map  $F$ . If  $M$  is a general Riemannian manifold of dimension  $d$  embedded in some  $\mathbb{R}^n$ ,  $r$  is now the product of the first  $d$  singular values of  $J$ . This coincides with the *pseudodeterminant* of  $J$ —the product of the non-zero singular values—as long as  $F$  is not degenerate.

In  $r$ -adaptive methods, controlling this area ratio is always a primary concern. An *equidistribution* principle is widely used: let  $m(\vec{x})$  be a suitable *monitor function*, traditionally related to the error in representing the solution on the physical mesh. We then seek a mesh where the area ratio is inversely proportional to  $m$ :

$$m(\vec{x})r(\vec{\xi}) = \alpha, \quad (2.3)$$

where  $\alpha$  is a normalisation constant that ensures the domains  $\Omega_C$  and  $\Omega_P$  have the correct size (alternatively, we could impose a condition on  $m$  to ensure the correct scaling). The error in representing the solution would then be *equidistributed* between cells of the physical mesh. The monitor function  $m$  does not have to be a proxy for interpolation error; a far more general monitor function can be used (for example, Weller et al. (2016) shows a mesh of the Earth adapted to the amount of precipitation that fell on a particular day). By eq. (2.3), if  $m(\vec{x})$  is large in a region, the cells of the physical mesh  $\tau_P$  are small there (as  $r(\vec{\xi})$  is forced to be small in the preimage of this region). This is desirable if higher resolution is sought in that area.

We refer to eq. (2.3) as the *equidistribution condition*. It is clear that it does not, on its own, lead to a well-posed mesh generation problem (other than in one-dimension), since the resulting map is far from unique. It is necessary to augment the equidistribution condition with further conditions. Traditionally, these have been constraints on mesh regularity such as orthogonality (Thompson et al., 1998) or alignment to a prescribed tensor field (Huang and Russell, 2011). In the latter approach, the resulting mesh is then chosen to minimise some weighted sum of terms, each attempting to enforce a separate condition. In particular, the mesh is not designed to satisfy eq. (2.3) exactly.

An alternative, and powerful, technique is to use the concept of *optimal transport* (Villani, 2003, 2009); previous work using this approach includes Budd and Williams (2006, 2009); Chacón et al. (2011); Browne et al. (2014). We now seek a map  $F$  satisfying eq. (2.3) exactly (up to discretisation error, at least) so that the resulting mesh  $\tau_P$  is “as close as possible” to  $\tau_C$ . This “distance” between the meshes is defined as

$$\int_{\Omega_C} \|\vec{x}(\vec{\xi}) - \vec{\xi}\|^2 d\vec{\xi}, \quad (2.4)$$

the integral of the squared Riemannian distance. In optimal transport terminology, this is the cost of a candidate map  $F : \Omega_C \rightarrow \Omega_P$ .

It is well-known that a unique solution exists for this problem; this was established in Brenier (1991) for Euclidean space and in McCann (2001) for the sphere. In Euclidean space, the

appropriate map can be written in the form

$$\vec{x} = F(\vec{\xi}) = \vec{\xi} + \nabla u, \quad (2.5)$$

for a suitable scalar ‘potential’  $u$ . The corresponding area ratio is

$$r(\vec{\xi}) = \det(I + H(u)), \quad (2.6)$$

where  $H(u)$  denotes the *Hessian* of  $u$ . In section 3, we extend this to the sphere. Combining eq. (2.3) with eq. (2.6) then leads to a nonlinear partial differential equation for  $u$ , a *Monge–Ampère* equation. Such equations, defined over general manifolds  $M$ , have been well-studied. Many results are available on the formal regularity of the solutions, including estimates for the various derivatives of the function  $u$  in terms of  $m$  (Trudinger and Urbas, 1984; Caffarelli, 1990; Wang, 1995; Gutiérrez, 2001; Delanoë and Loeper, 2006; Caffarelli et al., 2008; Loeper, 2009, 2011). The formal regularity properties of the resulting mesh  $\tau_P$  can then be determined from these estimates.

## 2.2. Geometrical measures

A general mesh  $\tau$  defined on a two-dimensional Riemannian manifold  $M$  is comprised of a set of nodes on  $M$  connected together by edges, defining a set of cells. In a well-behaved mesh, the nodes are regularly spaced and the edges meet at carefully-controlled angles. The resulting cells are therefore not too skew. The spherical meshes mentioned previously have these desirable properties, as does the uniform mesh on the plane. In an  $r$ -adaptive context, such meshes are appropriate for a computational mesh  $\tau_C$ . Under the action of the map  $F$ , the physical mesh  $\tau_P$  is typically less regular than  $\tau_C$ . In particular, the equidistribution condition eq. (2.3) controls the size of the mesh cells; if this varies, it leads to a degree of skewness in the mesh. A general criticism of  $r$ -adaptive meshes is that they can lead to excessively skew meshes. It can, however, be shown that the use of the optimal transport regularisation condition (which forces  $\tau_P$  to be “as close as possible” to  $\tau_C$ ) is beneficial for controlling the degree of skewness (Delzanno et al., 2008).

Assume that we are constructing meshes on a two-dimensional manifold. Let the map  $F : \Omega_C \rightarrow \Omega_P$  have Jacobian  $J$ . This linear operator has leading singular values  $\sigma_1, \sigma_2$ . We can then define the *local scaling* and *local skewness* in terms of these.

**Definition 1.** For the map  $F$ , the *local scaling*  $s$  is defined as

$$s = \sigma_1 \sigma_2, \quad (2.7)$$

while the *local skewness*  $Q$  is defined as

$$Q = \frac{1}{2} \left( \frac{\sigma_1}{\sigma_2} + \frac{\sigma_2}{\sigma_1} \right). \quad (2.8)$$

If  $F$  is the identity, so that the physical mesh is equal to the computational mesh,  $s$  is constant and  $Q = 1$ . However, for an adapted mesh, both will vary. The local scaling  $s$  is controlled directly via the equidistribution condition eq. (2.3). In contrast, the local skewness follows indirectly from properties of the Monge–Ampère equation. We will consider using the local skewness as a general measure of the quality of the mesh. In Huang and Russell (2011), it is shown how the interpolation error for a mesh, using different types of interpolant, can be calculated directly in terms of  $s$  and  $Q$ .

We remark that on the plane  $\mathbb{R}^2$ , the use of optimal transport techniques leads to  $J$  being symmetric, and so the expressions above in eqs. (2.7) and (2.8) can be written with eigenvalues replacing singular values. However, this is not true for a general manifold embedded in Euclidean space. We also remark that the measure of skewness above is based only on the linearisation of the map  $F$ . There are many other measures of mesh quality; some are used in Weller et al. (2016) and are based on larger scale properties of the mesh. These essentially require the analysis of higher-order terms in the expansion of  $F$ . However, we do not consider these in this paper.

### 3. Optimally transported meshes on the sphere

#### 3.1. Definition

As shown in McCann (2001), an optimal transport map on a manifold can again be expressed in terms of the gradient of a scalar function defined on the manifold. Let  $M$  be a general Riemannian manifold and  $u(\vec{\xi}) : M \rightarrow \mathbb{R}$  be the scalar ‘potential’ generated by the optimal transport procedure. We then define the *McCann map* as an *exponential map*  $F : M \rightarrow M$ :

$$\vec{x} = F(\vec{\xi}) = e^{\nabla u} \vec{\xi}. \quad (3.1)$$

The quantity  $\nabla u(\vec{\xi})$  lies in the cotangent space at  $\vec{\xi}$ , which can be trivially associated with the tangent space  $T_{\vec{\xi}}M$ . The exponential map maps this onto  $M$  itself. Intuitively, one selects the geodesic that passes through  $\vec{\xi}$  and coincides with  $\nabla u$  there, then travels a distance  $|\nabla u|$  along this geodesic. The expression eq. (3.1) reduces to the earlier expression eq. (2.5) if  $M$  is some  $\mathbb{R}^n$ .

From optimal transport theory, the function  $u$  automatically inherits a convexity property: it is  $c$ -convex, as defined in McCann (2001), where  $c$  denotes the cost function used for optimal transport. According to McCann (2001) (see also Loeper (2011)), if the monitor function  $m$  is sufficiently smooth then so is the potential  $u$ , and so the map eq. (3.1) is well-defined and locally bijective. The McCann map thus associates a well-defined map from  $M$  to  $M$  with the scalar-valued function  $u(\xi)$ .

Conversely, suppose we use eq. (2.1) to associate an area map  $r(\xi)$  with a general map  $F : M \rightarrow M$ . McCann (2001) showed that if  $r(\xi)$  is absolutely continuous with respect to the Lebesgue measure on  $M$ —which is certainly true if the monitor function  $m$  is continuous and

bounded away from zero—then there exists a unique optimal transport map of the form eq. (3.1) with this associated area map.

If  $M = S^2$ , the unit sphere, the geodesics are segments of great circles, and the resulting exponential map in eq. (3.1) can be calculated easily. Indeed, it can be written in closed form as

$$\vec{x} = \cos(\delta) \vec{\xi} + \sin(\delta) \frac{\nabla u}{|\nabla u|}, \quad \delta = |\nabla u|, \quad (3.2)$$

or, equivalently,

$$\vec{x} = \cos(\delta) \vec{\xi} + \frac{\sin(\delta)}{\delta} \nabla u, \quad \delta = |\nabla u|. \quad (3.3)$$

This is a simple case of Rodrigues' rotation formula. The form eq. (3.2) makes it clear that the destination  $\vec{x}$  is an appropriate combination of orthogonal unit vectors, while the alternative form eq. (3.3) highlights the reduction to the planar expression eq. (2.5) in the small- $\delta$  limit. We use these closed-form expressions for all our subsequent calculations on  $S^2$ .

### 3.2. Formal local and global regularity

In a series of papers (extending earlier work of, among others, Pogorelov, Lions, Gilbarg, Trudinger, and Urbas in  $\mathbb{R}^n$ ), Loeper (Loeper, 2011) and McCann (McCann, 2001) have derived estimates for the derivatives of the McCann map acting on  $S^2$ . These can be used to help determine the mesh regularity through eq. (2.8). The principal results from this work are summarised as follows.

**Theorem 1.** (Trudinger et al.) *Suppose that  $u$  satisfies a Monge–Ampère equation in Euclidean space of the form*

$$\det(I + H(u)) = g(\xi, \nabla u) \equiv 1/m(\xi, \nabla u). \quad (3.4)$$

*There then exists a constant  $C$  that depends only on  $g$ , the domain  $\Omega_C$ , and any boundary conditions, such that*

$$\sup_{\Omega_C} |H(u)| \leq C. \quad (3.5)$$

This result is then extended by Loeper:

**Theorem 2.** (Loeper) *Suppose that  $u$  is the solution of a problem of Monge–Ampère-type on the sphere, arising from an optimal transport problem as defined earlier. As long as  $g > 0$  (i.e.,  $m > 0$ ), then*

1. *if  $g \in C^{1,1}$  then  $u \in C^{3,\alpha}$ , and*
2. *if  $g \in C^\infty$  then  $u \in C^\infty$ .*

These results are significant for our mesh generation problem: the map from the computational domain  $\Omega_C$  to the physical domain  $\Omega_P$  is given by the exponential map of the gradient of  $u$ . The smoothness of  $u$  therefore implies smoothness of the map. We can deduce that if

$g \in C^\infty$ , the map is a  $C^\infty$ -function of  $\xi$ . Consequently, the singular values  $\sigma_j$  of the Jacobian of the map are bounded, differentiable functions of  $\xi$  over  $S^2$ . It follows further from the convexity properties that both  $\sigma_1$  and  $\sigma_2$  are uniformly bounded away from zero. We deduce from this that the skewness  $Q$  of the mesh is a bounded, differentiable function of  $\xi$  over  $S^2$ . Intuitively, we expect that the mesh we generate cannot become too skew.

It is shown further by Loeper that the formal regularity of  $u$  is slightly better on the sphere than for the plane. This is because the *cost-sectional curvature*—defined in Loeper (2011) and closely related to the usual curvature—is uniformly positive on the sphere, but is zero on the plane. In fact, it is possible to get certain formal regularity results on the sphere even if the source measure vanishes. On the sphere we also avoid problems on the plane, seen in Budd et al. (2015), where the mesh loses regularity as one approaches the boundary. In section 6, we make a direct comparison between the sphere and the plane.

### 3.3. A local coordinate-based approach

It is helpful to see how the exponential map can be expressed in terms of a *local* two-dimensional coordinate basis mapping from  $\mathbb{R}^2$  to  $S^2$ . A natural basis to use is spherical angles  $(\theta, \phi)$  with respect to some (unit) axis  $\vec{\omega}$ . This maps a coordinate patch  $(\theta, \phi) \in \mathbb{R}^2$  directly onto  $S^2$ . We can then consider—locally, at least— $u \equiv u(\theta, \phi)$ . To avoid singularities in the coordinate mapping, we will assume that we are working in a region well-separated from the poles  $\pm\vec{\omega}$ .

In this local basis, we have

$$\vec{\xi} = (\sin \theta \cos \phi, \sin \theta \sin \phi, \cos \theta)^T, \quad (3.6)$$

with local unit vectors

$$\vec{e}_\theta = (\cos \theta \cos \phi, \cos \theta \sin \phi, -\sin \theta)^T, \quad \vec{e}_\phi = (-\sin \phi, \cos \phi, 0)^T; \quad (3.7)$$

these are orthogonal and also orthogonal to  $\vec{\xi}$ . We then have

$$\nabla u = u_\theta \vec{e}_\theta + \frac{u_\phi}{\sin \theta} \vec{e}_\phi, \quad (3.8)$$

where, by assumption, we are working on a patch where  $\sin \theta$  is bounded away from zero. Note that, using the relation  $\cos \theta = \vec{\xi} \cdot \vec{\omega}$ , we can express these vectors as

$$\vec{e}_\theta = \frac{\cos(\theta) \vec{\xi} - \vec{\omega}}{\sin \theta}, \quad \vec{e}_\phi = \vec{\xi} \times \vec{e}_\theta = -\frac{\vec{\xi} \times \vec{\omega}}{\sin \theta}. \quad (3.9)$$

We can then substitute eq. (3.8) into eq. (3.3) to find the McCann map explicitly:

$$\vec{x} = \cos(\delta) \vec{\xi} + \frac{\sin(\delta)}{\delta} \left( u_\theta \vec{e}_\theta + \frac{u_\phi}{\sin \theta} \vec{e}_\phi \right), \quad \delta = \sqrt{u_\theta^2 + \left( \frac{u_\phi}{\sin \theta} \right)^2}. \quad (3.10)$$

The map eq. (3.10) induces a map on the local coordinate space from  $(\theta, \phi) \rightarrow (\theta', \phi')$ . It follows from standard geometry that the area ratio is

$$r(\vec{\xi}) = \frac{\sin \theta'}{\sin \theta} |K|, \quad \text{where } K = \frac{\partial(\theta', \phi')}{\partial(\theta, \phi)}. \quad (3.11)$$



After some manipulation, it follows from eq. (3.10) that

$$\cos \theta' = \cos \delta \cos \theta - \frac{\sin(\delta)}{\delta} \sin(\theta) u_\theta, \quad \sin(\phi' - \phi) = \frac{\sin(\delta) u_\phi}{\delta \sin \theta' \sin \theta} \quad (3.12)$$

The scaling factor  $r$  can then be derived by differentiating eq. (3.12) and applying eq. (3.11).

### 3.4. Summary

The formulation described in section 3.1 has several advantages for mesh generation. Firstly, we need only work with scalar quantities—monitor functions  $m$  and mesh potentials  $u$ —in order to compute the map  $\vec{x}(\vec{\xi})$ . Secondly, there is a substantial body of theory giving formal regularity estimates for solutions of the optimal transportation problem, as mentioned in section 3.2. This can be exploited to give formal regularity properties for the map and hence the mesh. Thirdly, provided the exponential map can be calculated easily (as on the sphere), it gives a systematic and straightforward way of finding a map  $M \rightarrow M$  which can be used to calculate the mesh in a natural manner, as opposed to some of the ad hoc approaches to mesh construction that can be found in the literature.

## 4. Exact axisymmetric maps

For general monitor functions, the optimal transport map cannot be expressed analytically. However, it is possible to create exact solutions for certain classes of examples. In Budd et al. (2015), exact solutions were developed for linear and radial features on the (periodic or infinite) plane. Here, we consider examples of axisymmetric monitor functions on the sphere. The action of these maps on certain computational meshes  $\tau_C$  can be studied, and the regularity of the resulting physical mesh  $\tau_P$  deduced. We can then obtain exact expressions for the scaling and skewness of the resulting meshes. We remark that if the axis of symmetry of the monitor function does not coincide with any axis of symmetry of the mesh  $\tau_C$ , the mesh  $\tau_P$  will not inherit any symmetry properties. For this section and the next, we only consider axisymmetric problems, and compare them to radially-symmetric maps on the plane in section 6. We return to the more general case in section 7.

### 4.1. Basic geometry

An axisymmetric function  $u$  satisfies  $u(\theta, \phi) \equiv u(\theta)$ , where the coordinates are defined with respect to some axis  $\vec{w}$ . We then have  $u_\phi = 0$ , so

$$\nabla u = u_\theta \vec{e}_\theta, \quad (4.1)$$

It then follows from eqs. (3.2) and (3.10) that

$$\vec{x} = \cos(\delta) \vec{\xi} + \frac{\sin(\delta)}{\delta} u_\theta \vec{e}_\theta, \quad \text{where } \delta = |u_\theta|. \quad (4.2)$$

It follows immediately from eq. (3.12) that if the local coordinates for  $\vec{\xi}$  are  $(\theta, \phi)$ , the new local coordinates  $(\theta', \phi')$  for  $\vec{x}$  are given by

$$\theta' = \theta + \frac{du}{d\theta}, \quad \phi' = \phi. \quad (4.3)$$

Thus, from eq. (3.11), the area scaling is given by

$$r(\theta, \phi) = \frac{\sin \theta' d\theta'}{\sin \theta d\theta} = \frac{\sin \theta'}{\sin \theta} (1 + u_{\theta\theta}). \quad (4.4)$$

It is also useful to also consider the axisymmetric map in a coordinate-free form. As before, let  $\vec{\omega}$  be the (unit) axis of symmetry. It follows from eq. (3.9) that

$$\nabla u = \frac{du}{d\theta} \frac{\cos(\theta) \vec{\xi} - \vec{\omega}}{\sin \theta} = (\theta' - \theta) \frac{\cos(\theta) \vec{\xi} - \vec{\omega}}{\sin \theta}. \quad (4.5)$$

Combining the previous results, we have

$$\vec{x} = \cos(\theta' - \theta) \vec{\xi} + \sin(\theta' - \theta) \frac{\cos(\theta) \vec{\xi} - \vec{\omega}}{\sin \theta}, \quad (4.6)$$

Using eqs. (4.3) and (4.6), we can generate a map  $\vec{x}(\vec{\xi})$  from the sphere to itself for any suitable  $u(\theta)$  and axis of symmetry  $\vec{\omega}$ .

## 4.2. Calculation of $\theta'$ from a monitor function

Consider an axisymmetric monitor function  $m(\vec{x}) \equiv m(\theta')$ , where  $\cos \theta' = \vec{x} \cdot \vec{\omega}$ . We can use the results of the previous subsection to calculate the map that equidistributes this monitor function. Using eq. (4.4), the equidistribution condition eq. (2.3) gives

$$m(\theta') \sin \theta' \frac{d\theta'}{d\theta} = \alpha \sin \theta \quad (4.7)$$

where  $\alpha$  is a normalisation constant. The axis of symmetry must map to itself, implying

$$\theta'(0) = 0, \quad \theta'(\pi) = \pi. \quad (4.8)$$

Integrating eq. (4.7), we have

$$F(\theta') \equiv \int_0^{\theta'} m(t) \sin t dt = \alpha(1 - \cos \theta), \quad (4.9)$$

where the normalisation constant  $\alpha$  satisfies

$$2\alpha = \int_0^\pi m(t) \sin t dt. \quad (4.10)$$

For particular monitor functions  $m(\theta')$ , we can use eqs. (4.7) to (4.10) to calculate  $\theta'$  directly from  $\theta$  by inverting  $F$ . Applying eq. (4.6) then lets us calculate  $\vec{x}(\vec{\xi})$  directly. We can apply this transformation to the vertices of some reasonably uniform mesh  $\tau_C$  to generate new meshes adapted to the given monitor function.

### 4.3. Local regularity

Two important mesh properties are its scale and regularity. Here, scale refers to the sizes of its cells, per eq. (2.7), and regularity to the skewness  $Q$  of cells, per eq. (2.8). Both of these are local measures of mesh quality, and relate to the resulting errors which can be expected when solving PDEs on the mesh. For these axisymmetric maps, we can obtain analytic expressions for the scale and skewness quantities in terms of the monitor function.

Consider a local quadrilateral coordinate patch in  $\mathbb{R}^2$  centred on  $(\theta, \phi)$  and of sides  $\delta\theta \times \delta\phi$ . This corresponds to a patch in  $S^2$  of sides  $\delta x \times \delta y = \sin\theta \delta\phi \times \delta\theta$ . The patch in  $\mathbb{R}^2$  is mapped to a patch centred on  $(\theta', \phi')$  of sides  $\delta\theta' \times \delta\phi'$ , which corresponds to a patch on  $S^2$  of sides  $\delta x' \times \delta y' = \sin\theta' \delta\phi' \times \delta\theta'$ . In the limit of the patch going to zero,

$$\frac{dx'}{dx} = \frac{\sin\theta'}{\sin\theta} \frac{d\phi'}{d\phi}, \quad \frac{dy'}{dy} = \frac{d\theta'}{d\theta}. \quad (4.11)$$

For an axisymmetric equidistribution map generated by the monitor function  $m(\theta')$ , eq. (4.7) implies

$$\frac{d\phi'}{d\phi} = 1, \quad \frac{d\theta'}{d\theta} = \frac{\alpha}{m(\theta')} \frac{\sin\theta}{\sin\theta'}. \quad (4.12)$$

Combining these, we have

$$\frac{dx'}{dx} = \frac{\sin\theta'}{\sin\theta}, \quad \frac{dy'}{dy} = \frac{\alpha}{m(\theta')} \frac{\sin\theta}{\sin\theta'}. \quad (4.13)$$

It follows that the Jacobian matrix  $J$  is diagonal and has eigenvalues

$$\lambda_1 = \frac{\sin\theta'}{\sin\theta}, \quad \lambda_2 = \frac{\alpha}{m(\theta')} \frac{\sin\theta}{\sin\theta'}. \quad (4.14)$$

Note that  $m\lambda_1\lambda_2 = \alpha$ , as required by the equidistribution condition eq. (2.3). From eq. (2.8), the local skewness of the axisymmetric map is given by

$$Q = \frac{1}{2} \left( \frac{\alpha}{m(\theta')} \frac{\sin^2\theta}{\sin^2\theta'} + \frac{m(\theta')}{\alpha} \frac{\sin^2\theta'}{\sin^2\theta} \right). \quad (4.15)$$

We now show that  $Q \rightarrow 1$  at the poles, as long as  $m$  is continuous. This implies that  $Q$  is close to unity for open regions around each pole. Therefore, the resulting mesh is extremely regular in these regions even if there is significant mesh contraction.

**Lemma 1.** *If  $m$  is continuous at the poles,  $Q \rightarrow 1$  as  $\theta' \rightarrow 0$  or  $\theta' \rightarrow \pi$ .*

*Proof.* It follows from the regularity of the map that  $d\theta'/d\theta$  exists. Furthermore, since  $\theta' = 0$  when  $\theta = 0$ , it follows that  $\sin\theta'/\sin\theta \rightarrow d\theta'/d\theta$  as  $\theta \rightarrow 0$ . Now, as in eq. (4.7), the equidistribution condition leads to

$$m \sin\theta' \frac{d\theta'}{d\theta} = \alpha \sin\theta. \quad (4.16)$$

It follows that, as  $\theta \rightarrow 0$ , we have

$$\frac{m \sin^2 \theta'}{\alpha \sin^2 \theta} \rightarrow \frac{m \sin \theta' \frac{d\theta'}{d\theta}}{\alpha \sin \theta} = 1. \quad (4.17)$$

Thus  $Q \rightarrow 1$ . A similar calculation can be performed for  $\theta \rightarrow \pi$ .  $\square$

The challenge of designing a mesh adaptation strategy can thus (at least locally) be summarised as an ODE-constrained optimisation problem. One must select monitor functions  $m(\theta')$  such that, with  $\theta'$  given by the differential equation

$$m(\theta') \sin \theta' \frac{d\theta'}{d\theta} = \alpha \sin \theta \quad (4.18)$$

and with the mesh skewness  $Q$  given by eq. (4.15), suitable bounds can be obtained for the maximum value of  $Q$ . We immediately see, stemming from the fact that  $S^2$  is compact and the result of lemma 1, that controlling the variation of  $Q$  is easier than on the plane.

## 5. Examples of exact axisymmetric solutions

In this section, we consider three types of axisymmetric monitor functions and the maps (and hence meshes) that these induce. The examples will be

1. Monitor functions for concentrating resolution in localised regions,
2. Monitor functions for zonal rings,
3. Monitor functions for point singularities.

We look at the action of the resulting maps on three types of meshes: a cubed-sphere mesh, an icosahedral mesh and a latitude–longitude mesh. We also calculate the resulting skewness for each type of monitor function.

The calculations in section 5.1, section 5.2 and section 5.3 make use of *SciPy* (Jones et al., 2001–), particularly the integration and optimisation routines. The calculations in section 5.4 and section 7 use the numerical methods developed in McRae et al. (2017), run with *Firedrake* (Rathgeber et al., 2016). These make use of specialist functionality developed in Rognes et al. (2013); Alnæs et al. (2014); McRae et al. (2016); Homolya and Ham (2016); Luporini et al. (2017); Homolya et al. (2017), and *Firedrake* itself relies on *PETSc* (Balay et al., 2016, 1997) and *petsc4py* (Dalcin et al., 2011).

### 5.1. Construction of the maps

For any axisymmetric monitor function  $m(\theta')$ , the formula eq. (4.9) can be used to evaluate the map  $\theta'(\theta)$ . We consider some monitor functions where the relevant integral can be calculated analytically, and so the map can be expressed in closed form. Unfortunately, these examples often lack regularity and will lead to meshes with sharp transitions. We therefore also consider

related, but smoother, monitor functions that lead to more practical meshes. These require the use of numerical quadrature.

### 5.1.1. Monitor functions for regions

We firstly consider monitor functions which concentrate points uniformly into regions, such as a disc centred on the axis  $\vec{\omega}$ . In a meteorology context, this could be used to represent a localised feature such as a hurricane. We consider a discontinuous “top-hat” monitor function, for which we can express the map analytically, and a smoothed version of this.

Our *top-hat* monitor function is given by the expression

$$m(\theta') = \begin{cases} \rho_1, & \theta' < \Theta' \\ \rho_2, & \theta' > \Theta', \end{cases} \quad (5.1)$$

where  $\Theta'$  marks the boundary between high- and low-resolution regions. The ratio  $\rho_1/\rho_2$  sets the ratio of mesh density between the two regions; we assume  $\rho_1 > \rho_2$ . The top-hat function is discontinuous, so formally we have less regularity than discussed in section 3.2, but the resulting optimal transport map is still continuous.

Integrating eq. (4.7) from the ‘boundaries’ 0 and  $\pi$ , we have

$$\rho_1(1 - \cos \theta') = \alpha(1 - \cos \theta), \quad \theta' < \Theta', \quad (5.2)$$

$$\rho_2(1 + \cos \theta') = \alpha(1 + \cos \theta), \quad \theta' > \Theta'. \quad (5.3)$$

It follows immediately from eq. (4.10) that the normalisation constant  $\alpha$  satisfies

$$2\alpha = \rho_1(1 - \cos \Theta') + \rho_2(1 + \cos \Theta'). \quad (5.4)$$

Finally, define  $\Theta$  to be the preimage of  $\Theta'$  under the map. By invoking continuity of the mesh, it follows that

$$\frac{\rho_1(1 - \cos \Theta')}{1 - \cos \Theta} = \frac{\rho_2(1 + \cos \Theta')}{1 + \cos \Theta}. \quad (5.5)$$

Using standard trigonometrical identities, this can be written

$$\rho_1 \tan^2(\Theta'/2) = \rho_2 \tan^2(\Theta/2). \quad (5.6)$$

Given a monitor function of the form eq. (5.1), we can find  $\Theta$  from  $\Theta'$  via eq. (5.6). We then apply eqs. (5.2) and (5.3) to find  $\theta'$  as a function of  $\theta$  in the separate ranges  $\theta < \Theta$  and  $\theta > \Theta$ . Having determined  $\theta'$ , we can calculate the image point  $\vec{x}$  for a given  $\vec{\xi}$  by using eq. (4.6). For example, if  $\rho_1 = 10, \rho_2 = 1$  and  $\Theta' = \pi/4$  then

$$\alpha \approx 2.318, \quad \Theta \approx 1.837. \quad (5.7)$$

The resulting map  $\theta \rightarrow \theta'$  is given in fig. 1.

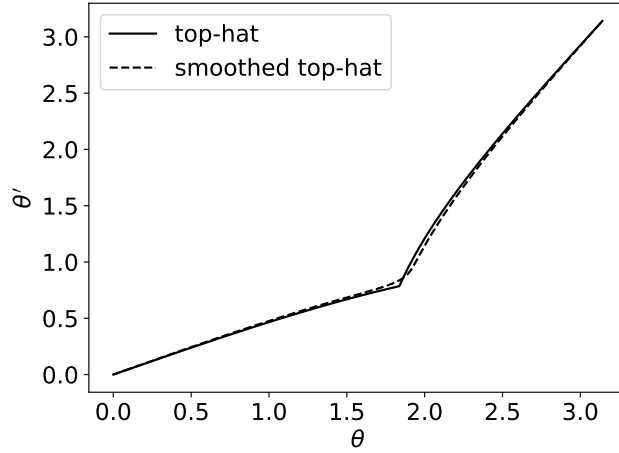


Figure 1: The map  $\theta'(\theta)$  produced by the top-hat monitor function eq. (5.1), with  $\rho_1/\rho_2 = 10$  and  $\Theta' = \pi/4$ , and by a smoothed approximation eq. (5.8), with  $\varepsilon = \pi/50$ . The top-hat monitor function has a discontinuity in  $m$ , which leads to a visible discontinuity in  $\frac{d\theta'}{d\theta}$ , per eq. (4.7). In the smoothed top-hat, the transition occurs over a distance  $\mathcal{O}(\varepsilon)$ .

We also consider a smoothed form of the top-hat monitor function, proposed by Ringler et al. (2011) in the context of a proposed global weather forecasting model with increased resolution over the United States<sup>1</sup>. This takes the form

$$m(\theta') = \sqrt{\frac{1-\gamma}{2} \left( \tanh\left(\frac{\Theta' - \theta'}{\varepsilon}\right) + 1 \right)} + \gamma, \quad (5.8)$$

where we assume  $\gamma$  is *small*. For small  $\theta'$ —the “inner region”—we have  $m(\theta') \approx 1$ , while for large  $\theta'$ ,  $m(\theta') \approx \sqrt{\gamma}$ . This monitor function therefore has a similar profile to the top-hat monitor function eq. (5.1), but with a smooth transition over a lengthscale  $\varepsilon$ . There is no closed-form integral of  $m(\theta') \sin(\theta')$ , so we cannot use eq. (4.9) to get a closed-form expression for  $\theta'(\theta)$ . However, we can use numerical quadrature to obtain an arbitrarily good approximation. We expect that it will have similar behaviour to the top-hat monitor function if the parameters are chosen carefully. We present a calculation for the smoothed monitor, taking  $\gamma = 1/10^2$ ,  $\Theta' = \pi/4$ , and  $\varepsilon = \pi/50$ , and the resulting map  $\theta \rightarrow \theta'$  is given in fig. 1.

### 5.1.2. Monitor functions for rings

Ring-like features arise in many applications, such as certain types of optical phenomena and also in low-amplitude Rossby waves. A monitor function which concentrates points in a ring on

<sup>1</sup>The expression in the original paper is incorrect; a correct version is given in our recent paper McRae et al. (2017), and is used here.

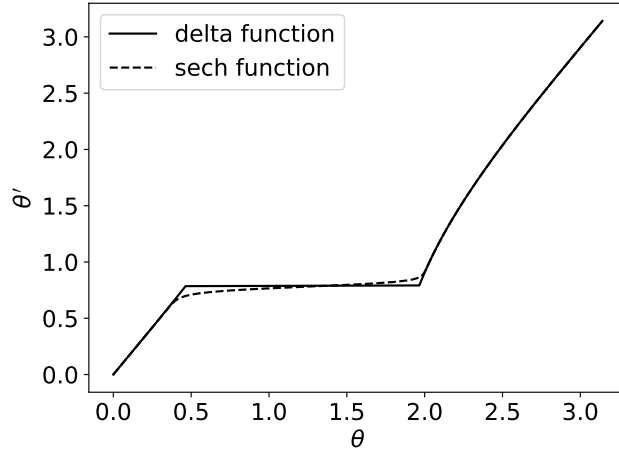


Figure 2: The map  $\theta'(\theta)$  produced by a ring monitor function based on a delta function eq. (5.10), with  $\gamma = 5$  and  $\Theta' = \pi/4$ , and one based on a smoother sech function eq. (5.9), with  $\varepsilon = \pi/50$ . For the delta-function-based monitor function, all  $\theta \in [\theta_1, \theta_2]$  are mapped to  $\Theta'$ . For the smoother approximation, the transition occurs over a distance (in  $\theta'$ ) of  $\mathcal{O}(\varepsilon)$ .

the sphere is given by

$$m(\theta') = 1 + \frac{\beta}{\varepsilon} \operatorname{sech}^2 \left( \frac{\theta'^2 - \Theta'^2}{\varepsilon} \right). \quad (5.9)$$

The ring is of width  $\mathcal{O}(\varepsilon)$ , where  $\varepsilon$  is assumed small, and is at an angle of  $\Theta'$  from the axis  $\vec{\omega}$ . The parameter  $\beta$  controls the density of mesh points in the ring. In the limit  $\varepsilon \rightarrow 0$ ,  $m$  approximates the delta function given by

$$m(\theta') = 1 + \gamma \delta(\theta' - \Theta'). \quad (5.10)$$

Here,  $\gamma$  controls the density of mesh points in the ring; in comparison with eq. (5.9),  $\gamma = \beta/\Theta'$  to leading order. The analysis of the monitor function eq. (5.10) is straightforward, although the resulting mesh transformation (or, rather, its inverse) is discontinuous. By eq. (4.10), we have

$$\alpha = 1 + \frac{\gamma}{2} \sin \Theta'. \quad (5.11)$$

Integrating from 0 and from  $\pi$ , we have

$$1 - \cos \theta' = \alpha(1 - \cos \theta), \quad \theta' < \Theta', \quad (5.12)$$

$$1 + \cos \theta' = \alpha(1 + \cos \theta), \quad \theta' > \Theta'. \quad (5.13)$$

We observe immediately that if  $\theta$  and  $\theta'$  are both close to 0 or are both close to  $\pi$ ,

$$\theta' \approx \sqrt{\alpha} \theta, \quad \text{or} \quad (\pi - \theta') \approx \sqrt{\alpha} (\pi - \theta). \quad (5.14)$$

This implies that the mesh is very regular close to the two poles of the axis, and is consistent with the result of lemma 1. The monitor function eq. (5.10) leads to a jump in the value of the computational coordinate  $\theta$  when the physical coordinate satisfies  $\theta' = \Theta'$ . If  $\theta_1$  and  $\theta_2$  are mapped to the inner and outer edge of the ring, so that  $\theta_1 \rightarrow \Theta'_-$  and  $\theta_2 \rightarrow \Theta'_+$ , then eqs. (5.12) and (5.13) give

$$\cos \theta_1 = 1 - \frac{1 - \cos(\Theta')}{\alpha}, \quad \cos \theta_2 = \frac{1 + \cos(\Theta')}{\alpha} - 1 \quad (5.15)$$

For example, if we take  $\Theta' = \pi/4$  and  $\gamma = 5$ ,

$$\theta_1 \approx 0.464, \quad \theta_2 \approx 1.964, \quad \alpha \approx 2.768, \quad (5.16)$$

and the resulting map is presented in fig. 2.

Returning to the smoother monitor function eq. (5.9), we take  $\Theta' = \pi/4$ ,  $\beta = 5\pi/4$  – compatible with the value of  $\gamma$  used in the delta function example – and  $\varepsilon = \pi/50$ . The relevant integrals are evaluated with numerical quadrature, and the resulting map is shown in fig. 2.

### 5.1.3. Monitor function for a point singularity

As a final example, we consider a monitor function that concentrates mesh cells around a single point. We use a monitor function that concentrates half of the mesh cells around the axis of symmetry, with increasing density towards the pole:

$$m(\theta') = \gamma e^{-\gamma(1-\cos \theta')} + \frac{1}{2}, \quad (5.17)$$

where  $\gamma$  is assumed to be large. Considering the small- $\theta'$  expansion of  $\cos \theta'$ , we see  $m(\theta')$  is a (scaled and translated) Gaussian in the vicinity of the point singularity.

Note that

$$\int_0^{\theta'} m(t) \sin t \, dt = 1 - e^{-\gamma(1-\cos \theta')} + \frac{1}{2}(1 - \cos \theta') \quad (5.18)$$

Therefore

$$\alpha = \frac{1}{2} (2 - e^{-2\gamma}), \quad (5.19)$$

which is approximately 1 for  $\gamma$  large. By eq. (4.9), the map  $\theta'(\theta)$  satisfies

$$1 - e^{-\gamma(1-\cos \theta')} + \frac{1}{2}(1 - \cos \theta') = \frac{1}{2} (2 - e^{-2\gamma}) (1 - \cos \theta). \quad (5.20)$$

The resulting map for  $\gamma = 100$  is presented in fig. 3. The graph has a distinct inner region, which is linear, a nonlinear outer region, and a transition close to the expected  $\theta = \pi/2$ .

Studying eq. (5.20) further, if  $\gamma$  is large and  $\theta'$  is not close to zero, discarding small terms and rearranging leads to

$$\cos \theta' \approx 1 + 2 \cos \theta, \quad (5.21)$$



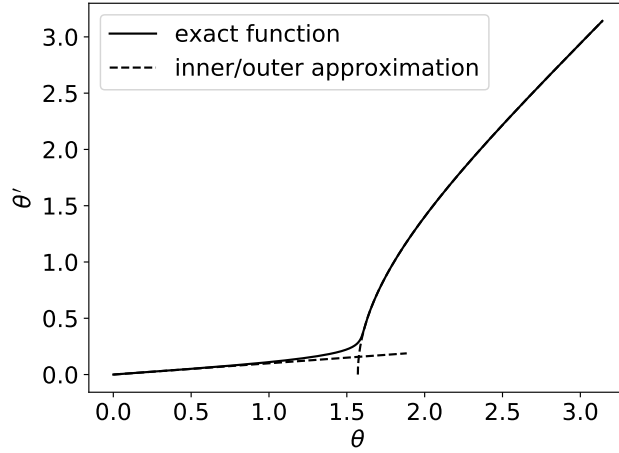


Figure 3: The map  $\theta'(\theta)$  generated by the “point singularity” monitor function eq. (5.17) with  $\gamma = 100$ . The asymptotic approximations eq. (5.21) and eq. (5.22) are also shown. In the limit  $\gamma \rightarrow \infty$ , half the mesh points are concentrated around the designated point (inner approximation), while the other half are spread evenly over the sphere (outer approximation).

valid for  $\theta > \pi/2 + o(1)$ . Notably, this is independent of  $\gamma$ . In the “inner region”, where  $\theta$  and  $\theta'$  are both small, we have

$$\theta' \approx \frac{\theta}{\sqrt{\gamma}}. \quad (5.22)$$

Combining these two results explains the approximate shape of the plot in fig. 3. We can estimate the value of  $\theta'$  where the transition occurs, say  $\theta'_*$ , by setting  $\theta = \pi/2$  in eq. (5.20). To leading order, this gives

$$1 - \cos \theta'_* = 2e^{-\gamma(1 - \cos \theta'_*)}. \quad (5.23)$$

Setting  $s = \gamma(1 - \cos \theta'_*)$  we have  $s/\gamma = 2e^{-s}$ . The solution to this can be expressed using the Lambert- $W$  function; for large  $\gamma$ ,  $s = \log(2\gamma) - \log \log(2\gamma) + o(1)$ . The leading-order approximation to  $\theta'_*$  is then

$$\theta'_* \approx \sqrt{\frac{2 \log(2\gamma)}{\gamma}}. \quad (5.24)$$

## 5.2. Local regularity of the maps

Having presented a range of monitor functions in the previous subsection, we now calculate the skewness function  $Q$  in each case and comment on the implications for mesh regularity.

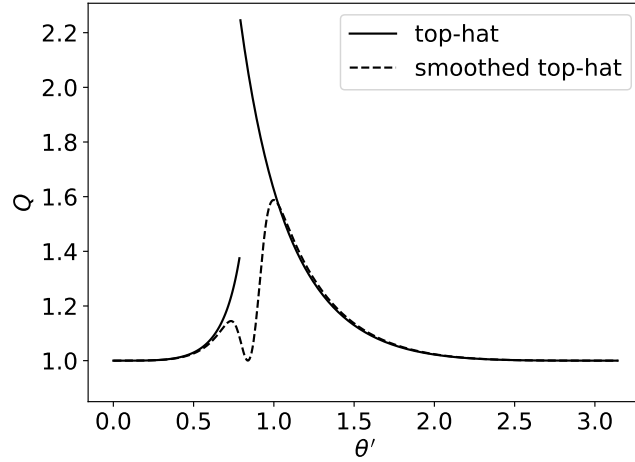


Figure 4: The skewness functions for the maps generated by the top-hat and smoothed top-hat monitor functions. For the top-hat monitor function,  $Q$  is maximised when approaching the transition from the outside; it can be shown analytically that the resulting  $Q_{\max} \approx 2.273$ . For the smoothed approximation,  $Q_{\max}$  is notably smaller, despite the maps in fig. 1 being very similar. Perhaps surprisingly,  $Q$  returns to 1 in the interior of the transition region; this can be attributed to continuity. For both monitor functions, as expected,  $Q \rightarrow 1$  at the poles.

### 5.2.1. Regions

We first consider the map induced by the top-hat monitor function eq. (5.1). It follows from eq. (4.15) that the local skewness of the map is given by

$$Q = \frac{1}{2} \left( \frac{\alpha \sin^2 \theta}{\rho_i \sin^2 \theta'} + \frac{\rho_i \sin^2 \theta'}{\alpha \sin^2 \theta} \right) \quad (5.25)$$

in each region  $i$ . In fig. 4, we plot  $Q$  as a function of  $\theta'$  for the case studied previously, where  $\rho_1/\rho_2 = 10$  and  $\Theta' = \pi/4$ . We see that  $Q$  takes its largest value just outside the “top-hat region”, *i.e.*, at  $\theta' = \Theta'_+$ . We therefore expect to see the most significant mesh distortion in this region, as was also observed in Weller et al. (2016). The value of  $Q_{\max}$ , approximately 2.273, implies the resulting mesh will have some *moderately* skewed cells.

We also consider the smoother top-hat monitor function eq. (5.8), with the same parameters as before. The resulting skewness factor is plotted in fig. 4. The skewness  $Q$  now takes its maximum value in the outer part of the transition region. Perhaps surprisingly,  $Q$  reaches 1 in the middle of the transition region, suggesting that the mesh is briefly very regular. This can be explained by continuity: approaching the transition from inside, the cells are stretched in one direction (zonally), but are stretched in the other direction (meridionally) when approaching from outside. By continuity, there must be some intermediate value of  $\theta'$  where the cells are stretched equally in both directions, so that  $Q = 1$ .

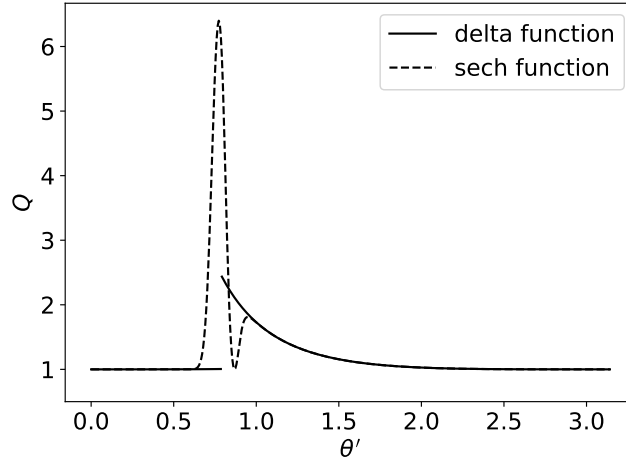


Figure 5: The skewness functions for the maps generated by the delta-function-based and sech-function-based monitor functions for ring-like features. For the delta-function example, we have not tried to represent the infinite skewness in the ring itself. The maximum skewness outside the ring is approximately 2.467. Intuitively, the ring ‘swallows’ cells due to the delta function. The remaining cells must then be stretched out to cover the entire area, leading to skewness. For the smooth example, the maximum skewness in the ring region is around 6.4. There is a secondary peak in  $Q$  outside the ring, as in the delta-function case, and  $Q$  briefly touches 1 due to continuity.

### 5.2.2. Rings

We firstly consider the smooth ring monitor function eq. (5.9) with the same parameters as before. The skewness factor is plotted in fig. 5. Again,  $Q$  is continuous, and unsurprisingly takes its maximum value inside the ring region. This value – close to 6.4, representing anisotropic stretching by a factor between 12 and 13 – is fairly moderate, given that the monitor function varies by a factor of 63.5. The resulting mesh cells are, as we will see later, well-aligned with the ring itself. Such a mesh is well-suited for representing a function that is aligned with the ring (Huang and Russell, 2011; Budd et al., 2017). The resulting interpolation error estimates will be lower, in this case, than those arising from a uniform mesh.

We also consider the delta function eq. (5.10) that this approaches in the limit  $\varepsilon \rightarrow 0$ . The resulting skewness factor is theoretically infinite in the ring, as cells have length zero in the meridional direction. However, the maximum skewness outside of this is just 2.467..., obtained by substituting  $m(\theta') = 1$ ,  $\theta' = \Theta'$ ,  $\theta = \theta_2$ , and  $\alpha$  in eq. (4.15). The values of  $\theta_2$  and  $\alpha$  for these parameters were given previously in eq. (5.16). The skewness factor is plotted in fig. 5.

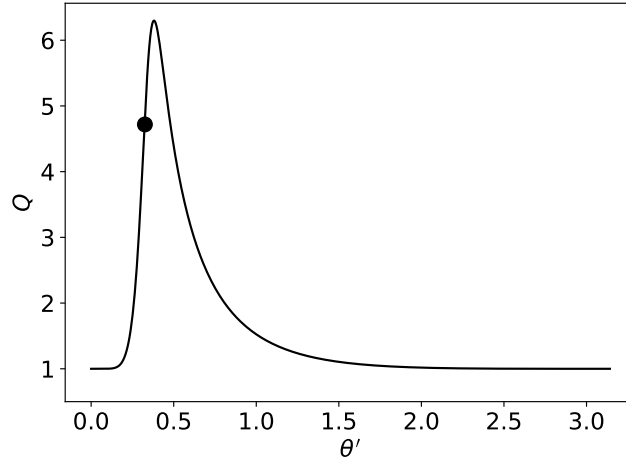


Figure 6: The skewness function for the map generated by the “point singularity” monitor function. The circle denotes the leading-order estimate to the transition location  $\theta'_*$ , per eq. (5.24), and the corresponding skewness estimate  $Q_*$ , per eq. (5.26), although there is no a priori reason to expect this to coincide with the peak of  $Q$ . As predicted,  $Q$  is close to unity at both poles, implying a regular grid. This is despite significant mesh compression near the singularity.

### 5.2.3. Point singularity

We consider the cosine-bell-like monitor function eq. (5.17) from before, with  $\gamma$  again set as 100. The resulting skewness  $Q(\theta')$  is plotted in fig. 6. The skewness is large in the transition region, and is maximised for  $\theta'$  close to (but somewhat larger than) the leading-order estimate eq. (5.24) for  $\theta'_*$ . The corresponding leading-order estimate for  $Q_* := Q(\theta'_*)$ , using eq. (4.15), is

$$Q_* \approx \frac{\gamma}{4 \log(2\gamma)}, \quad (5.26)$$

and this is marked in fig. 6.

### 5.3. Meshes induced by the maps

We now present meshes adapted to the various types of monitor function we considered previously. These are produced by applying the resulting axisymmetric maps to various “computational” meshes  $\tau_C$ . We will compare the resulting meshes with the skewness calculations in the previous subsection. Note that our definition of the skewness, as in eq. (2.8), is a property of the *map*, not of the meshes themselves. However, as long as  $\tau_C$  is reasonably uniform and has regular angles, large skewness values will coincide with highly-skewed cells in the adapted mesh  $\tau_P$ .

For clarity, the adapted meshes are generated as follows. The geometry and topology of the

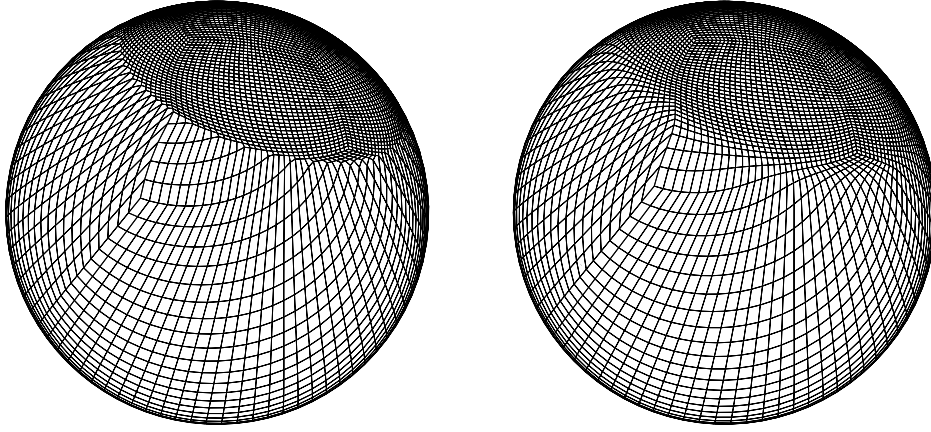


Figure 7: A cubed-sphere mesh, adapted to the top-hat and smoothed top-hat monitor functions.

computational mesh  $\tau_C$  is assumed to be known, as is the monitor function axis  $\vec{\omega}$  (taken to have unit length) and the map  $\theta'(\theta)$ . Consider some vertex of  $\tau_C$ , located at  $\vec{\xi} \in S^2$ . We can calculate the corresponding value of  $\theta$ , since  $\cos \theta = \vec{\xi} \cdot \vec{\omega}$ , and hence the value of  $\theta'$  for the image point  $\vec{x}$ . We can then use the expression eq. (4.6) to determine  $\vec{x}$  explicitly – it is on the same great circle as  $\vec{\omega}$  and  $\vec{\xi}$ , and is at an angle  $\theta'$  from  $\vec{\omega}$  (on the same “side” as  $\vec{\xi}$ ). This is performed for each vertex of  $\tau_C$ ; the image vertices form the adapted mesh  $\tau_P$ , which has the same connectivity as  $\tau_C$ .

For ease of visualisation, the axis of rotational symmetry,  $\omega$ , is always taken to be proportional to  $(0.7, -1.0, 2.0)^T$ , and the meshes are viewed from the negative-y direction. This allows the mesh behaviour around the pole  $\omega$ , and in any “inner region”, to be seen clearly. The mesh behaviour around the opposite pole,  $-\omega$ , cannot be seen directly, but (in all cases that we use) it is visible that the mesh is becoming increasingly regular towards the pole. The computational meshes each have some rotational symmetry about the z-axis  $(0.0, 0.0, 1.0)^T$ . However, they have no symmetry about  $\omega$ , the symmetry axis of the monitor function. This is done deliberately, in order to illustrate more general behaviour.

### 5.3.1. Regions

We firstly show meshes adapted to the top-hat and smoothed top-hat monitor functions. Figure 7 shows the effect of the resulting maps on a cubed-sphere mesh, made up of six patches of ‘squares’, while fig. 8 shows the same for an icosahedral mesh, formed of triangles. In each case, the high concentration of mesh points in the inner region is clear. We also see, as predicted, good regularity of the meshes near the poles, which follows from  $Q$  approaching unity there.

The meshes produced by the top-hat monitor function have a visible sharp transition at  $\theta' = \Theta'$ ; this is rather smoother for the tanh-based monitor function. As predicted, there is a narrow

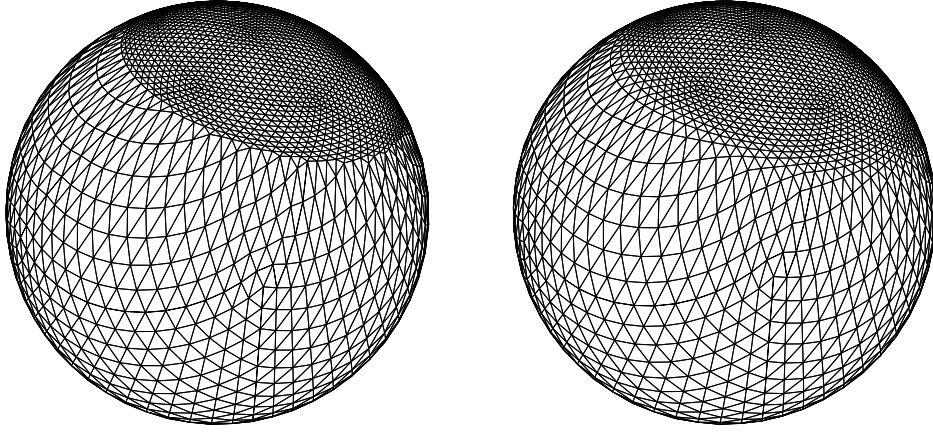


Figure 8: An icosahedral mesh, adapted to the top-hat and smoothed top-hat monitor functions.

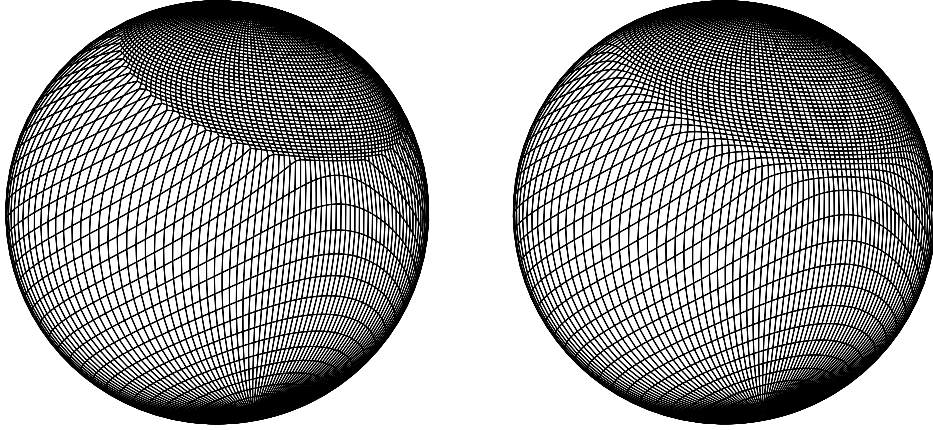


Figure 9: A latitude–longitude mesh, adapted to the top-hat and smoothed top-hat monitor functions.

band of ‘regular’ cells in the transition region, where  $Q \approx 1$ . In general, these meshes are suitable for a computation; if desired, the transition could be further smoothed by increasing  $\varepsilon$ .

We also consider the map applied to a latitude–longitude mesh, which already has a large variation in cell-size. The resulting mesh is shown in fig. 9. This no longer has orthogonal grid lines, one of the main advantages of the latitude–longitude mesh, and has maintained the disadvantage of large variations in cell-size. This mesh is unlikely to be useful for numerical weather prediction calculations, and the cubed-sphere or icosahedral meshes are probably far more suitable.

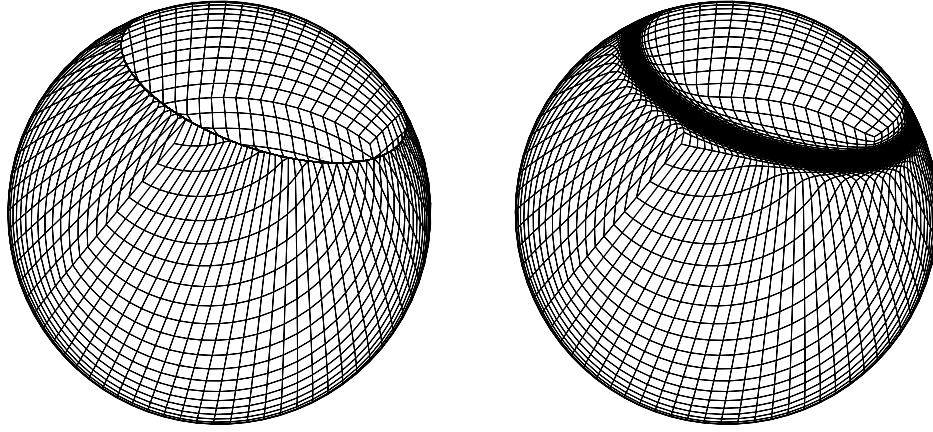


Figure 10: A cubed-sphere mesh, adapted to the delta-function-based and sech-function-based ring monitor functions.

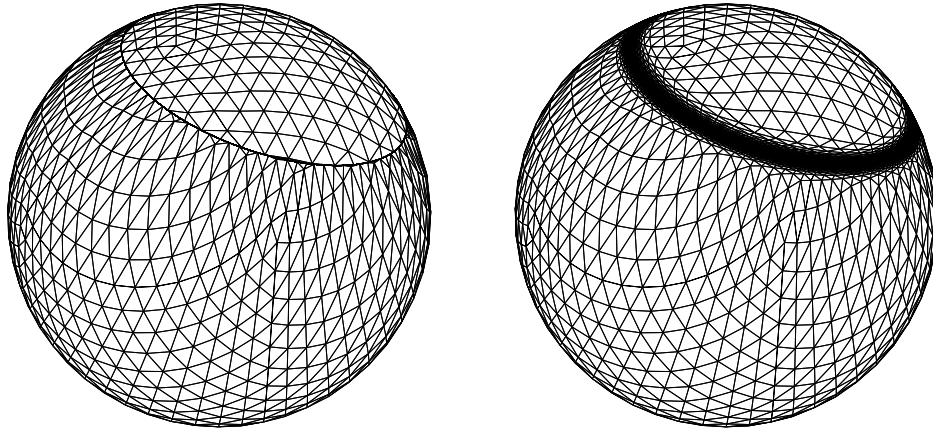


Figure 11: An icosahedral mesh, adapted to the delta-function-based and sech-function-based ring monitor functions.

### 5.3.2. Rings

We next show meshes adapted to the delta-function-based and sech-function-based ring monitor functions. Cubed-sphere meshes are shown in Figure 10, while icosahedral meshes are shown in fig. 11. While the meshes adapted to delta functions are obviously unsuitable for calculations, outside the singular ring they are remarkably similar to those adapted to the corresponding sech function. The smoother meshes are, as predicted, quite skew in the ring region. However, it is well-aligned with the ring itself, which is likely *beneficial* for representing a ring-like feature.

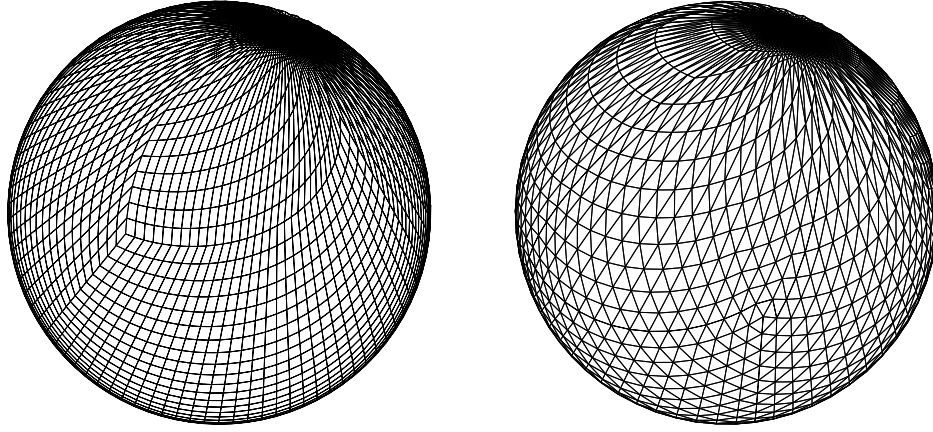


Figure 12: Cubed-sphere and icosahedral meshes, adapted to the monitor function for a point singularity.

### 5.3.3. Point singularity

We finally show meshes adapted to the monitor function for a point singularity. Cubed-sphere and icosahedral meshes are shown in fig. 12. As expected, the meshes are regular around the poles. There is a noticeable amount of stretching in the middle region, however, as predicted by the skewness calculation fig. 6.

## 5.4. Numerical skewness calculations

In section 7, we will apply the numerical methods developed in McRae et al. (2017) in order to generate non-axisymmetric examples. We firstly apply this approach to axisymmetric examples so that we can compare the output to the ‘analytic’ results we have obtained so far.

For an analytically prescribed monitor function, the numerical method produces the physical mesh coordinate field  $\vec{x}$ . This lives in the finite element space  $(P_2)^3$  – calculations are done with the sphere immersed in  $\mathbb{R}^3$ . The corresponding coordinate field for the computational mesh is denoted  $\vec{\xi}$ . We define the raw Jacobian  $J$  as the  $L^2$ -projection of  $\nabla_{\vec{\xi}} \vec{x}$  into  $(P_2)^{3 \times 3}$ . Analytically, the column space of  $J$  would have no component normal to the sphere, but this is not true in the presence of discretisation errors. We therefore form  $J' = (I - \vec{x}\vec{x}) \cdot J$  to eliminate this component completely. At each node, we then perform an SVD:  $J' = U\Sigma V$ . The matrix  $\Sigma$  is a diagonal matrix containing the singular values of the map  $\sigma_1, \sigma_2$ , and a third entry  $\sigma_3 \approx 0$ . The first column of  $U$ ,  $\vec{u}_1$ , is a vector in the direction of maximum local stretching, while  $\vec{u}_2$  is at right angles to this. The vectors  $\sigma_1 \vec{u}_1$  and  $\sigma_2 \vec{u}_2$  therefore represent the local stretching of the mesh.

We show the skewness quantity  $Q$ , together with the vectors  $\sigma_1 \vec{u}_1$  and  $\sigma_2 \vec{u}_2$ , for several of the examples considered previously. For brevity, we use an icosahedral mesh in each case.



Figure 13 shows the tanh-based region example, fig. 14 shows the sech-based ring example, and fig. 15 shows the point singularity example.

The results are largely as expected. It can be seen that the vectors  $\vec{u}_1$  and  $\vec{u}_2$  generally point towards the pole and perpendicular to it, a consequence of the axisymmetry of the examples. This is occasionally violated in the regions where  $Q \approx 1$ , in which there is no dominant direction of local stretching. The maximum skewness is somewhat underestimated in the point singularity example. This is perhaps not surprising: the large skewness is caused by stretching of cells in the meridional direction. The meridional resolution is therefore poor precisely where the skew is large, and fairly large discretisation errors can be expected. Using a once-refined mesh (not shown) gives the closer estimate of 5.59.

## 6. A comparison with meshes on the plane

We briefly compare the regularity of a mesh on the sphere with an ‘equivalent’ mesh on a subset of the plane, extending the analysis in Budd et al. (2015). On the plane, we consider a radially-symmetric monitor function, which induces a map  $R(r)$  from computational space to physical space. The equidistribution condition then leads to

$$m(R) \frac{dR}{dr} R = \alpha r, \quad (6.1)$$

where  $\alpha$  is again a normalisation constant. This can be compared with eq. (4.7) for the sphere. For a disc of radius  $\pi$ ,  $\alpha$  satisfies

$$\frac{1}{2} \alpha \pi^2 = \int_0^\pi m(R) R dR, \quad (6.2)$$

c.f. eq. (4.10). In Budd et al. (2015), it is shown that the eigenvalues of the map are  $dR/dr$  and  $R/r$ . By following similar steps to section 4.3, the skewness  $Q$  is given by

$$Q = \frac{1}{2} \left( \frac{\alpha}{m(R)} \left( \frac{r}{R} \right)^2 + \frac{m(R)}{\alpha} \left( \frac{R}{r} \right)^2 \right). \quad (6.3)$$

For  $r$  and  $R$  small, we have  $R/r \rightarrow dR/dr$  as  $r \rightarrow 0$ . As on the sphere, it follows that

$$Q \rightarrow 1 \quad \text{as} \quad r, R \rightarrow 0, \quad (6.4)$$

and hence the mesh is very regular in this limit. However, as we approach the boundary (which we assume is mapped to itself –  $R(a) = a$ ), we have

$$Q = \frac{1}{2} \left( \frac{\alpha}{m(a)} + \frac{m(a)}{\alpha} \right), \quad (6.5)$$

This value is completely arbitrary; there is no control over  $Q$  as we approach the boundary, and the mesh could be very skew there, as was observed in Budd et al. (2015). This could not occur on the sphere.

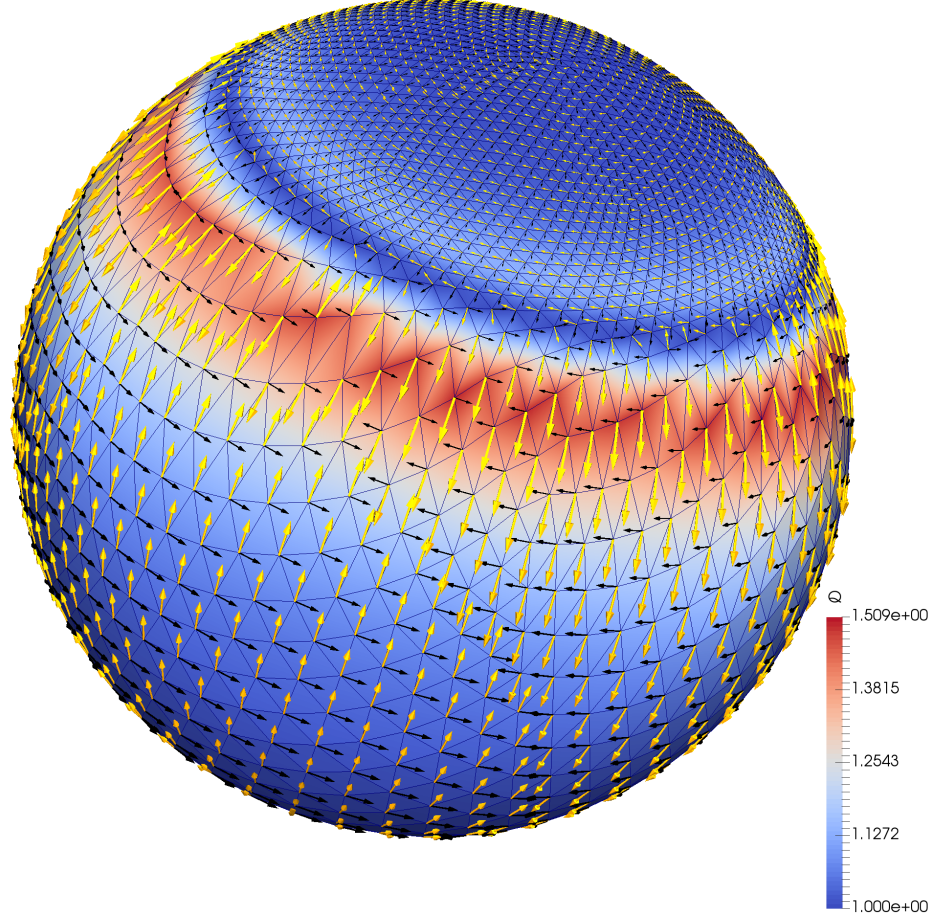


Figure 13: Numerical skewness calculation for the tanh-based region monitor function. The background colour shows the skewness,  $Q$ , while the arrows represent the scaled singular vectors  $\sigma_1 \vec{u}_1$  (orange) and  $\sigma_2 \vec{u}_2$  (black). The ‘flipping’ of arrows between neighbouring cells is an artifact of the sign-ambiguity of the SVD, and is not supposed to be physically significant. It is clear that  $Q$  approaches 1 at the poles  $\pm \vec{\omega}$ . The maximum skewness is found just outside the high-resolution region, as predicted by fig. 4, and the intermediate band of  $Q = 1$  is visible. In the outer region, there is meridional stretching, so the leading singular vector is in the meridional direction. In the inner region, there is meridional compression, so the leading singular vector is in the zonal direction.

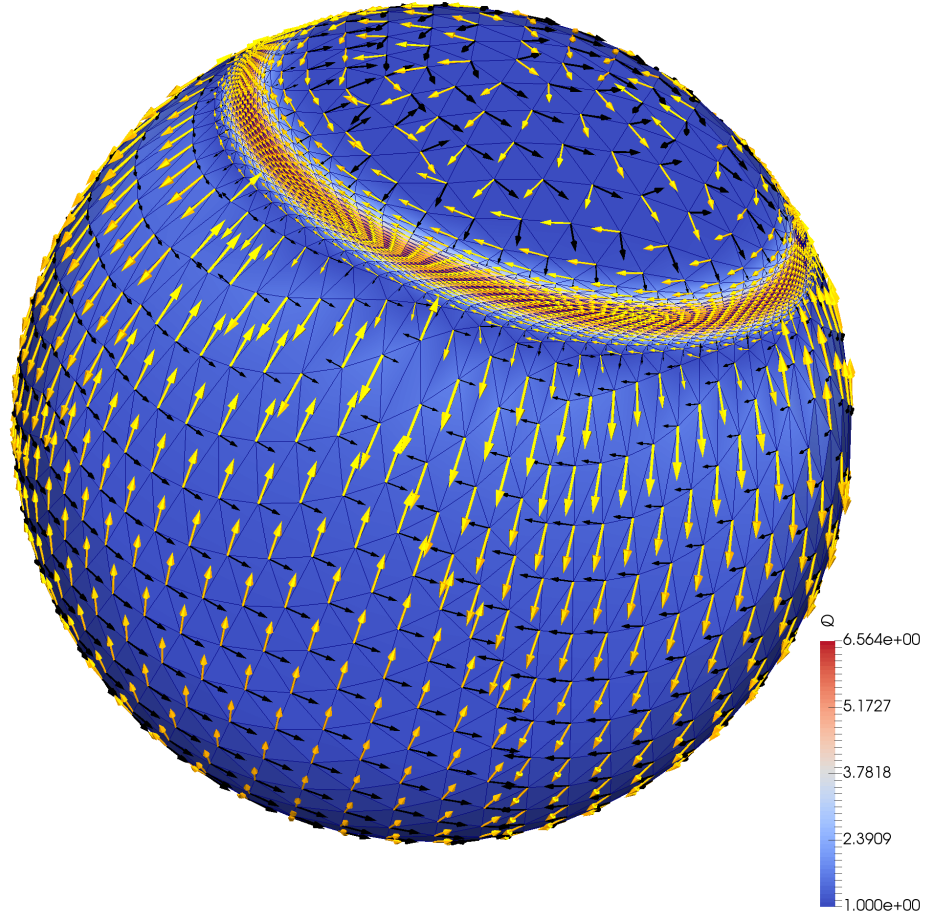


Figure 14: As fig. 13, for the sech-based ring monitor function. The maximum skewness is found in the high-resolution ring, and is close to the earlier prediction of approximately 6.4. The return to  $Q = 1$  is visible as a darker blue band just outside the ring. Within the ring, there is extreme meridional compression, so the leading singular vector is in the zonal direction. Outside the ring, there is mild meridional stretching, so the leading singular vector is in the meridional direction.

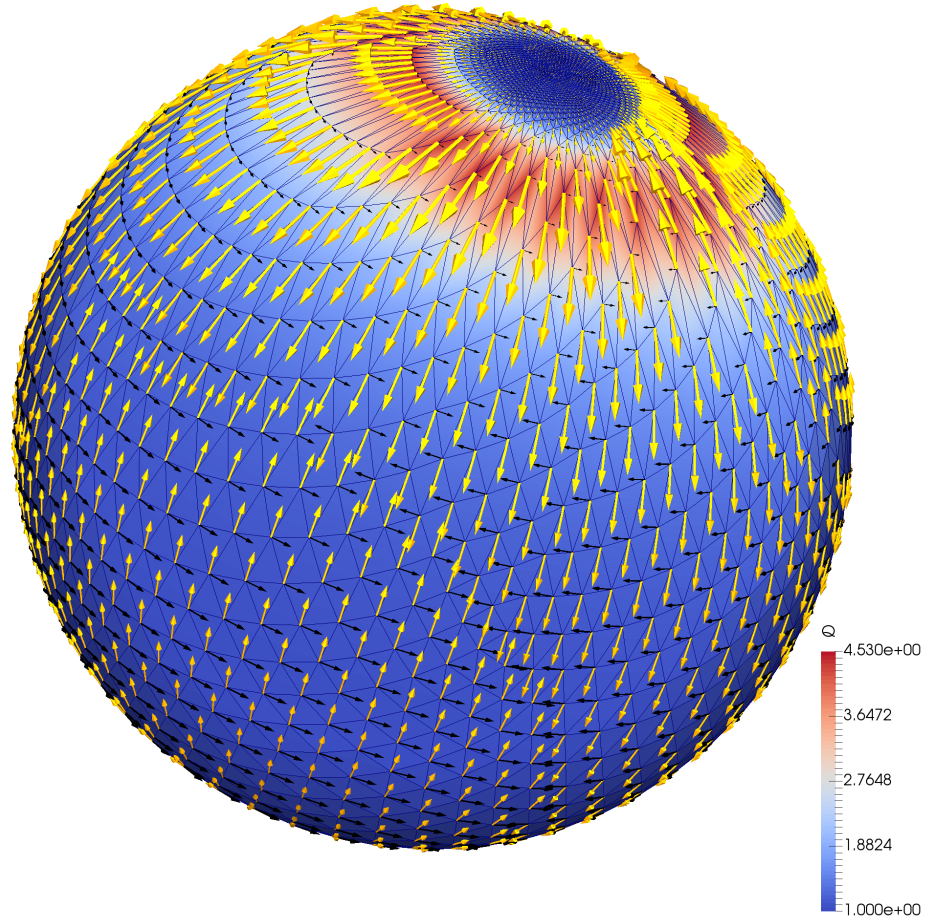


Figure 15: As fig. 13, for the point singularity monitor function. As predicted in fig. 6, there is minimal skew in the inner region, and the maximum skewness is found just outside the inner region. The leading singular vector is in the meridional direction everywhere; unlike the other examples, there is no transition.

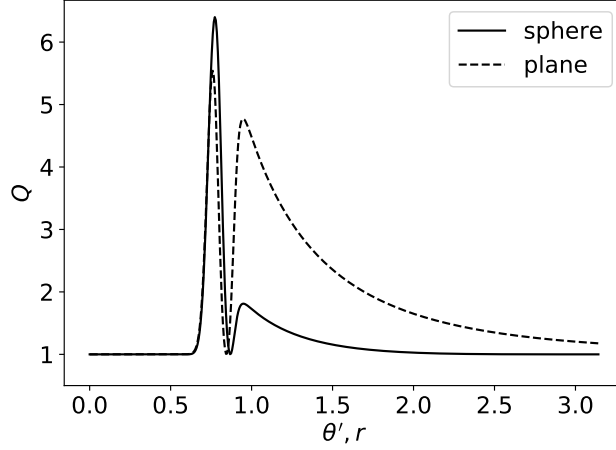


Figure 16: The skewness functions for the maps generated by the sech-based ring monitor function on the sphere and on the plane. Both cases lead to large skewness in the ring itself, which is expected, and is likely to be desirable. However, the differing geometries result in the plane having a far larger secondary peak than the sphere. This secondary peak corresponds to cells outside the ring being radially stretched in order to cover the remaining area.

To give a specific numerical example, consider the sech-based ring monitor function eq. (5.9),

$$m(\theta') = 1 + \frac{\beta}{\varepsilon} \operatorname{sech}^2 \left( \frac{\theta'^2 - \Theta'^2}{\varepsilon} \right), \quad (6.6)$$

together with an ‘equivalent’ radially-symmetric monitor function for a disk of radius  $\pi$ ,

$$m(R) = 1 + \frac{\beta}{\varepsilon} \operatorname{sech}^2 \left( \frac{R^2 - \Theta'^2}{\varepsilon} \right). \quad (6.7)$$

As in section 5.1, we take  $\Theta' = \pi/4$ ,  $\beta = 5\pi/4$ , and  $\varepsilon = \pi/50$ . The resulting skewness is shown in fig. 16. Both cases naturally lead to large skew in the ring itself. However, the secondary peak is much larger in the planar case than for the sphere, corresponding to (unwanted) radial stretching of cells. This is consistent with the mesh shown in Fig 4.3 of Budd et al. (2015).

## 7. More general meshes

In the previous sections, we considered several numerical examples that made use of axisymmetric monitor functions. With the axisymmetric restriction, the equidistribution requirement eq. (2.3) reduces to a one-dimensional ODE eq. (4.7). This could be solved to an effectively arbitrary degree of accuracy, and, in some cases, exactly. We were therefore able to make precise statements about the geometry of the resulting meshes. Without the axisymmetric restriction,

the equidistribution requirement and the optimal transport condition lead to a PDE. This can be expressed with respect to spherical angles, as in section 3.3, or with respect to the background Cartesian space  $\mathbb{R}^3$ , as was done in McRae et al. (2017). We now repeat the skewness calculations from section 5.4 for some non-axisymmetric examples. Again, we solve the PDE numerically, using the methods described in McRae et al. (2017).

Our first example is shown in fig. 17. The monitor function is formed of two intersecting ring features, and is based on (though different to) the ‘cross’ example in McRae et al. (2017). The monitor function is given by

$$m(\vec{x}) = \prod_i^N (1 + \alpha_i \operatorname{sech}^2(\beta_i(\|\vec{x} - \omega_i\|^2 - (\pi/2)^2))). \quad (7.1)$$

We take  $N = 2$ ,  $\alpha_1 = \alpha_2 = 5$ ,  $\beta_1 = \beta_2 = 5$ , and the axes  $\omega_1, \omega_2 = (\pm\sqrt{3}/2, 0, 1/2)$  are such that the rings cross at an angle of 60 degrees. The mesh cells in the ring are reasonably skewed, as expected, while the cells outside the ring are almost unaffected. Notably, where the rings intersect, the skewness is small, and the mesh is very well-behaved there.

Our second example is shown in fig. 18. The monitor function concentrates cells within a sinusoidal pattern in the northern hemisphere. It is inspired by the related planar example in Budd et al. (2015), and is not dissimilar to a Rossby–Hauritz wave (see, for example, test case 6 from Williamson et al. (1992)). The monitor function is given by

$$m(\vec{x}) = 1 + \alpha \operatorname{sech}(\beta \theta'), \quad \theta' = \theta - (\theta_c + \frac{1}{2} \theta_a \sin(k\phi)), \quad (7.2)$$

where  $\theta$  is the latitude (now measured from the equator),  $\phi$  is the longitude,  $\alpha = 15$ ,  $\beta = 25$ ,  $\theta_c = \frac{\pi}{6}$ ,  $\theta_a = \frac{\pi}{6}$ , and we use a wavenumber  $k = 3$ . The mesh cells are well-aligned with the sinusoidal pattern. There is only slight stretching of cells outside this high-resolution region.

Our final example is shown in fig. 19. The monitor function consists of two cosine bells, and is based on the initial condition for a spherical advection test case in Nair and Lauritzen (2010). The monitor function is given by

$$m(\vec{x}) = 1 + \frac{1}{2} \alpha \left( \sum_i 1 + \cos \left( \frac{\pi r_i(\vec{x})}{r} \right) \right), \quad (7.3)$$

where  $\alpha$  is the ‘strength’, taken to be 8, and  $r$  is the ‘width’ of each cosine bell, taken to be 0.5. We define  $r_i(\vec{x}) = \min(r, d_i(\vec{x}))$ , with  $d_i(\vec{x})$  denoting the great-circle distance from  $\vec{x}$  to the centre of cosine bell  $i$ . We place one cosine bell each side of the equator, centred at latitudes  $\pm \frac{\pi}{6}$ . Within the cosine bells, the mesh is very regular. There is mild stretching around the high-resolution regions. However, the significant stretching in the small region between the two cosine bells is likely undesirable.

## 8. Conclusions

In this paper, we have given a generic method that produces adapted meshes on the sphere. These are topologically identical to the (presumably fairly uniform) input mesh. This involves



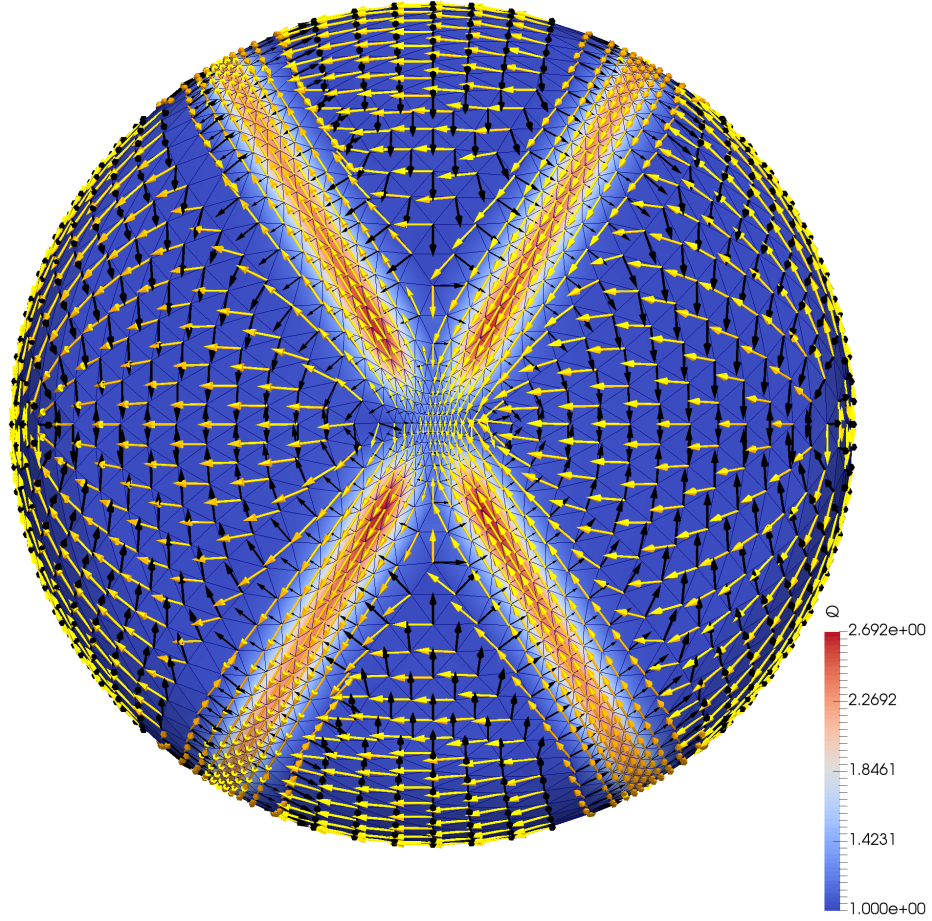


Figure 17: As fig. 13, for the ‘cross’ monitor function eq. (7.1). The mesh is well-aligned to the intersecting ring features. Within the rings, the dominant singular vector is in the direction of the ring. Away from the cross, the mesh undergoes very mild stretching in order to ‘provide’ resolution to the ring features.

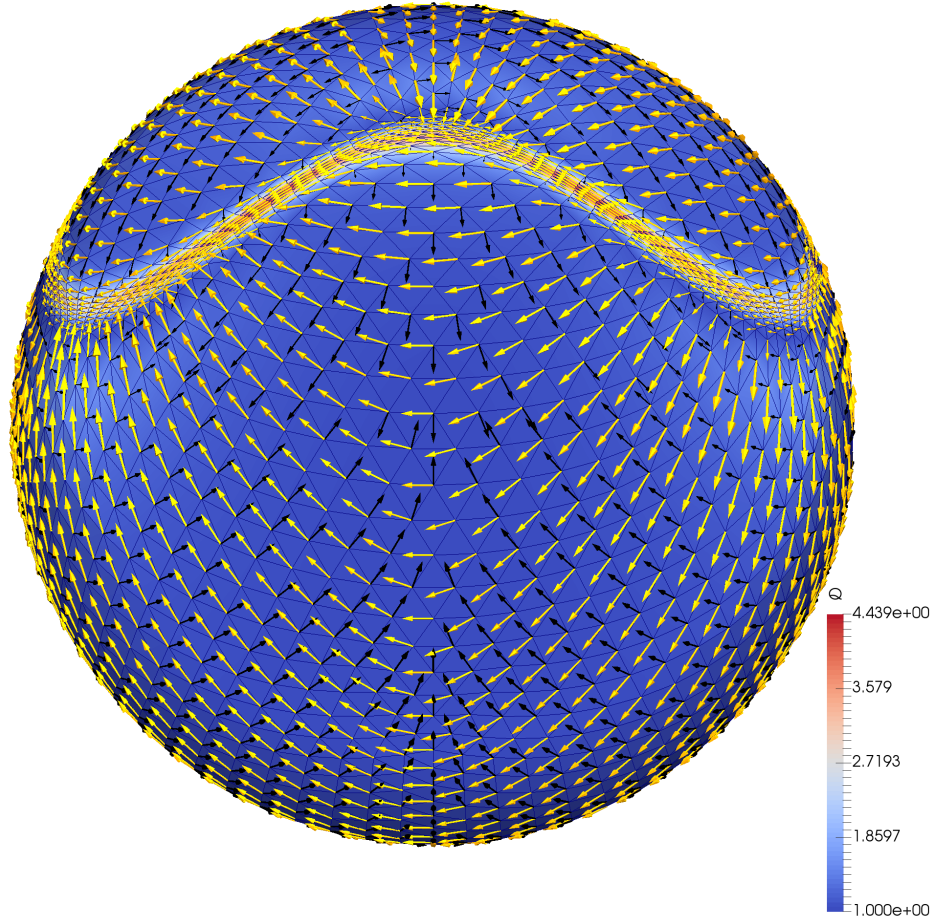


Figure 18: As fig. 13, for the sinusoidal monitor function eq. (7.2). The dominant singular vectors show that the mesh is very well aligned to the sinusoidal feature. There is some mild stretching of the mesh immediately outside the feature in order to provide the enhanced resolution. Away from the feature, the mesh is incredibly regular.



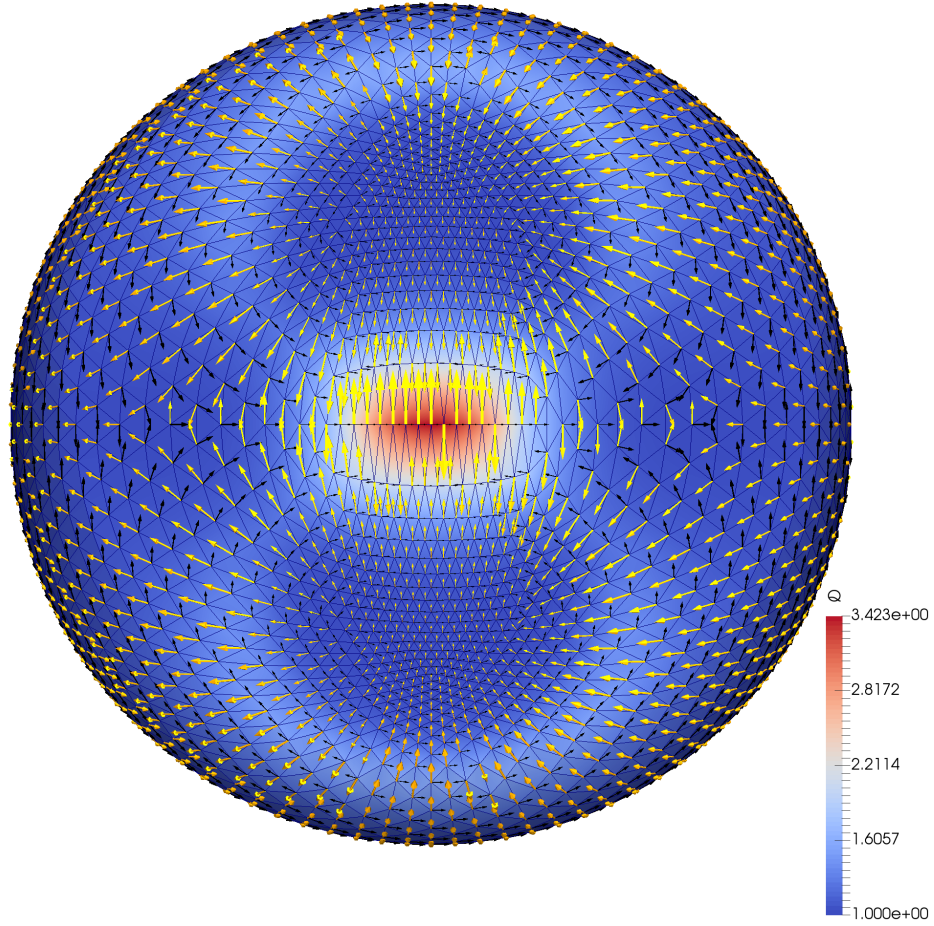


Figure 19: As fig. 13, for the monitor function eq. (7.3), representing two cosine bells. The mesh is very regular within the cosine bells, and there is some mild stretching immediately outside the cosine bells in order to provide the required resolution. Unfortunately, there is significant stretching in the zone between the cosine bells, where resolution is being demanded from both sides. In order to preserve the area of these cells, they are then compressed in the other direction, which exacerbates the skewness quantity.

calculating a map from the sphere to itself, and applying this map to the input mesh. By using an optimal transport strategy to find this map, we have a robust method of constructing such a mesh. Furthermore, various mesh regularity properties are inherited from the regularity of the map.

The map can be obtained as the solution of a PDE of Monge–Ampère type. By looking at a particular class of solutions, we analytically derived some specific maps and their associated skewness properties, and hence various meshes which could be used for computations. We also considered more general examples, calculating the maps and meshes numerically, and showed that the resulting meshes still have good regularity properties. As on the plane, we observed that the meshes generated through the optimal transport approach are capable of producing anisotropic meshes, even though the monitor function is only scalar-valued.

Of course, for useful problems, finding a mesh is just one part of solving a physical problem, perhaps represented by a PDE. The equation must then be discretised on the mesh (using, for example, a finite volume or finite element approach). There are numerous issues that must still be investigated. In the context of advection-dominated flows, this includes the accuracy and stability of the solution, the dispersion relations of any waves, the ability of the mesh to support balanced flows, and the construction of suitable monitor functions to achieve these. This ongoing research will be the subject of future papers.

## Acknowledgements

The authors would like to thank Hilary Weller and Jemma Shipton for useful discussions about mesh properties, and William Saunders for help producing vector graphics. This work was supported by the Natural Environment Research Council [grant numbers NE/M013480/1, NE/M013634/1].

## A. Code availability

All of the numerical experiments given in this paper were performed with the following versions of software, which we have archived on Zenodo: Firedrake (Zenodo/Firedrake), PyOP2 (Zenodo/PyOP2), TSFC (Zenodo/TSFC), COFFEE (Zenodo/COFFEE), UFL (Zenodo/UFL), FInAT (Zenodo/FInAT), FIAT (Zenodo/FIAT), PETSc (Zenodo/PETSc), petsc4py (Zenodo/petsc4py). The code for the numerical experiments can be found in the supplementary material to this paper.

## References

Martin S. Alnæs, Anders Logg, Kristian B. Ølgaard, Marie E. Rognes, and Garth N. Wells. Unified Form Language: A Domain-Specific Language for Weak Formulations of Partial Differential Equations. *ACM Transactions on Mathematical Software*, 40(2):9:1–9:37, 2014. doi: 10.1145/2566630.

- Satish Balay, William D. Gropp, Lois Curfman McInnes, and Barry F. Smith. Efficient Management of Parallelism in Object Oriented Numerical Software Libraries. In E. Arge, A. M. Bruaset, and H. P. Langtangen, editors, *Modern Software Tools in Scientific Computing*, pages 163–202. Birkhäuser Press, 1997.
- Satish Balay, Shrirang Abhyankar, Mark F. Adams, Jed Brown, Peter Brune, Kris Buschelman, Lisandro Dalcin, Victor Eijkhout, William D. Gropp, Dinesh Kaushik, Matthew G. Knepley, Lois Curfman McInnes, Karl Rupp, Barry F. Smith, Stefano Zampini, Hong Zhang, and Hong Zhang. PETSc Users Manual. Technical Report ANL-95/11 - Revision 3.7, Argonne National Laboratory, 2016. URL <http://www.mcs.anl.gov/petsc>.
- Gheorghe-Teodor Bercea, Andrew T. T. McRae, David A. Ham, Lawrence Mitchell, Florian Rathgeber, Luigi Nardi, Fabio Luporini, and Paul H. J. Kelly. A structure-exploiting numbering algorithm for finite elements on extruded meshes, and its performance evaluation in Firedrake. *Geoscientific Model Development*, 9(10):3803–3815, 2016. doi: 10.5194/gmd-9-3803-2016.
- Yann Brenier. Polar Factorization and Monotone Rearrangement of Vector-Valued Functions. *Communications on Pure and Applied Mathematics*, 44(4):375–417, 1991. doi: 10.1002/cpa.3160440402.
- P.A. Browne, C.J. Budd, C. Piccolo, and M. Cullen. Fast three dimensional r-adaptive mesh redistribution. *Journal of Computational Physics*, 275:174–196, 2014. doi: 10.1016/j.jcp.2014.06.009.
- C J Budd and J F Williams. Parabolic Monge–Ampère methods for blow-up problems in several spatial dimensions. *Journal of Physics A: Mathematical and General*, 39(19):5425–5444, 2006. doi: 10.1088/0305-4470/39/19/S06.
- C. J. Budd and J. F. Williams. Moving Mesh Generation Using the Parabolic Monge–Ampère Equation. *SIAM Journal on Scientific Computing*, 31(5):3438–3465, 2009. doi: 10.1137/080716773.
- C.J. Budd, R.D. Russell, and E. Walsh. The geometry of r-adaptive meshes generated using optimal transport methods. *Journal of Computational Physics*, 282:113–137, 2015. doi: 10.1016/j.jcp.2014.11.007.
- C.J. Budd, R.D. Russell, and E. Walsh. Near optimal mesh generation using optimal transport based methods. *In preparation*, 2017.
- Luis A. Caffarelli. Interior  $W^{2,p}$  estimates for solutions of the Monge–Ampère equation. *Annals of Mathematics*, 131(1):135–150, 1990. doi: 10.2307/1971510.
- Luis A. Caffarelli, Cristian E. Gutiérrez, and Qingbo Huang. On the regularity of reflector antennas. *Annals of Mathematics*, 167(1):299–323, 2008. doi: 10.4007/annals.2008.167.299.
- L. Chacón, G.L. Delzanno, and J.M. Finn. Robust, multidimensional mesh-motion based on Monge–Kantorovich equidistribution. *Journal of Computational Physics*, 230(1):87–103, 2011. doi: 10.1016/j.jcp.2010.09.013.

- Lisandro D. Dalcin, Rodrigo R. Paz, Pablo A. Kler, and Alejandro Cosimo. Parallel distributed computing using Python. *Advances in Water Resources*, 34(9):1124–1139, 2011. doi: 10.1016/j.advwatres.2011.04.013.
- Philippe Delanoë and Grégoire Loeper. Gradient estimates for potentials of invertible gradient-mappings on the sphere. *Calculus of Variations and Partial Differential Equations*, 26(3):297–311, 2006. doi: 10.1007/s00526-006-0006-4.
- G.L. Delzanno, L. Chacón, J.M. Finn, Y. Chung, and G. Lapenta. An optimal robust equidistribution method for two-dimensional grid adaptation based on Monge–Kantorovich optimization. *Journal of Computational Physics*, 227(23):9841–9864, 2008. doi: 10.1016/j.jcp.2008.07.020.
- Cristian E. Gutiérrez. *The Monge-Ampère Equation*. Birkhäuser Boston, Boston, MA, 2001. ISBN 978-1-4612-6656-3. doi: 10.1007/978-1-4612-0195-3.
- M. Homolya and D. A. Ham. A parallel edge orientation algorithm for quadrilateral meshes. *SIAM Journal on Scientific Computing*, 38(5):S48–S61, 2016. doi: 10.1137/15M1021325.
- Miklós Homolya, Lawrence Mitchell, Fabio Luporini, and David A. Ham. TSFC: a structure-preserving form compiler. *Submitted to SIAM Journal on Scientific Computing*, 2017. URL <https://arxiv.org/abs/1705.03667>.
- Weizhang Huang and Robert D. Russell. *Adaptive Moving Mesh Methods*. Applied Mathematical Sciences. Springer Science+Business Media, LLC, 2011. ISBN 978-1-4419-7915-5. doi: 10.1007/978-1-4419-7916-2.
- Eric Jones, Travis Oliphant, Pearu Peterson, et al. SciPy: Open Source Scientific Tools for Python, 2001–. URL <http://www.scipy.org/>. [Online; accessed 2017-06-26].
- Grégoire Loeper. On the regularity of solutions of optimal transportation problems. *Acta Mathematica*, 202(2):241–283, 2009. doi: 10.1007/s11511-009-0037-8.
- Grégoire Loeper. Regularity of Optimal Maps on the Sphere: the Quadratic Cost and the Reflector Antenna. *Archive for Rational Mechanics and Analysis*, 199(1):269–289, 2011. doi: 10.1007/s00205-010-0330-x.
- Fabio Luporini, David A. Ham, and Paul H. J. Kelly. An algorithm for the optimization of finite element integration loops. *ACM Transactions on Mathematical Software*, 44(1):3:1–3:26, 2017. doi: 10.1145/3054944.
- Alexander E. MacDonald, Jacques Middlecoff, Tom Henderson, and Jin-Luen Lee. A general method for modeling on irregular grids. *International Journal of High Performance Computing Applications*, 25(4):392–403, 2010. doi: 10.1177/1094342010385019.
- Robert J. McCann. Polar factorization of maps on Riemannian manifolds. *Geometric And Functional Analysis*, 11(3):589–608, 2001. doi: 10.1007/PL00001679.

- A. T. T. McRae, G.-T. Bercea, L. Mitchell, D. A. Ham, and C. J. Cotter. Automated generation and symbolic manipulation of tensor product finite elements. *SIAM Journal on Scientific Computing*, 38(5):S25–S47, 2016. doi: 10.1137/15M1021167.
- Andrew T. T. McRae, Colin J. Cotter, and Chris J. Budd. Optimal-transport-based mesh adaptivity on the plane and sphere using finite elements. *Submitted to SIAM Journal on Scientific Computing*, 2017. URL <https://arxiv.org/abs/1612.08077>.
- Ramachandran D. Nair and Peter H. Lauritzen. A class of deformational flow test cases for linear transport problems on the sphere. *Journal of Computational Physics*, 229(23):8868–8887, 2010. doi: 10.1016/j.jcp.2010.08.014.
- Florian Rathgeber, David A. Ham, Lawrence Mitchell, Michael Lange, Fabio Luporini, Andrew T. T. McRae, Gheorghe-Teodor Bercea, Graham R. Markall, and Paul H. J. Kelly. Firedrake: Automating the Finite Element Method by Composing Abstractions. *ACM Transactions on Mathematical Software*, 43(3):24:1–24:27, 2016. doi: 10.1145/2998441.
- Todd D. Ringler, Doug Jacobsen, Max Gunzburger, Lili Ju, Michael Duda, and William Skamarock. Exploring a Multiresolution Modeling Approach within the Shallow-Water Equations. *Monthly Weather Review*, 139(11):3348–3368, 2011. doi: 10.1175/MWR-D-10-05049.1.
- M. E. Rognes, D. A. Ham, C. J. Cotter, and A. T. T. McRae. Automating the solution of PDEs on the sphere and other manifolds in FEniCS 1.2. *Geoscientific Model Development*, 6(6): 2099–2119, 2013. doi: 10.5194/gmd-6-2099-2013.
- Andrew Staniforth and John Thuburn. Horizontal grids for global weather and climate prediction models: a review. *Quarterly Journal of the Royal Meteorological Society*, 138(662):1–26, 2012. doi: 10.1002/qj.958.
- Joe F. Thompson, Bharat K. Soni, and Nigel P. Weatherill, editors. *Handbook of grid generation*. CRC Press, 1998. ISBN 9780849326875.
- Neil S. Trudinger and John I.E. Urbas. On second derivative estimates for equations of Monge-Ampère type. *Bulletin of the Australian Mathematical Society*, 30(3):321–334, 1984. doi: 10.1017/S0004972700002069.
- Cédric Villani. *Topics in Optimal Transportation*. Graduate Studies in Mathematics. American Mathematical Society, 2003. ISBN 978-0-8218-3312-4.
- Cédric Villani. *Optimal Transport: Old and New*. Grundlehren der mathematischen Wissenschaften. Springer-Verlag Berlin Heidelberg, Berlin, Heidelberg, 2009. ISBN 978-3-540-71049-3. doi: 10.1007/978-3-540-71050-9.
- Xu-Jia Wang. Some counterexamples to the regularity of Monge-Ampère equations. *Proceedings of the American Mathematical Society*, 123(3):841–845, 1995. doi: 10.1090/S0002-9939-1995-1223269-0.

- Hilary Weller, Philip Browne, Chris Budd, and Mike Cullen. Mesh adaptation on the sphere using optimal transport and the numerical solution of a Monge–Ampère type equation. *Journal of Computational Physics*, 308:102–123, 2016. doi: 10.1016/j.jcp.2015.12.018.
- David L. Williamson. The Evolution of Dynamical Cores for Global Atmospheric Models. *Journal of the Meteorological Society of Japan*, 85B:241–269, 2007. doi: 10.2151/jmsj.85B.241.
- David L. Williamson, John B. Drake, James J. Hack, Rüdiger Jakob, and Paul N. Swartztrauber. A Standard Test Set for Numerical Approximations to the Shallow Water Equations in Spherical Geometry. *Journal of Computational Physics*, 102(1):211–224, 1992. doi: 10.1016/S0021-9991(05)80016-6.
- Zenodo/COFFEE. COFFEE: A Compiler for Fast Expression Evaluation, May 2017. URL <https://doi.org/10.5281/zenodo.573267>.
- Zenodo/FIAT. FIAT: The Finite Element Automated Tabulator, October 2017. URL <https://doi.org/10.5281/zenodo.1022075>.
- Zenodo/FInAT. FInAT: a smarter library of finite elements, October 2017. URL <https://doi.org/10.5281/zenodo.1022065>.
- Zenodo/Firedrake. Firedrake: an automated finite element system, October 2017. URL <https://doi.org/10.5281/zenodo.1022074>.
- Zenodo/PETSc. PETSc: Portable, Extensible Toolkit for Scientific Computation, October 2017. URL <https://doi.org/10.5281/zenodo.1022071>.
- Zenodo/petsc4py. petsc4py: The Python interface to PETSc, October 2017. URL <https://doi.org/10.5281/zenodo.1022068>.
- Zenodo/PyOP2. PyOP2: Framework for performance-portable parallel computations on unstructured meshes, October 2017. URL <https://doi.org/10.5281/zenodo.1022070>.
- Zenodo/TSFC. TSFC: The Two Stage Form Compiler, October 2017. URL <https://doi.org/10.5281/zenodo.1022066>.
- Zenodo/UFL. UFL: The Unified Form Language, October 2017. URL <https://doi.org/10.5281/zenodo.1022069>.